# Flow Failure Assessment for Dams and Embankments

Timothy D. Stark
Department of Civil and Environmental Engineering
University of Illinois at Urbana-Champaign
205 N. Mathews Ave.
Urbana, IL 61801
(217) 333-7394
tstark@Illinois.edu

and

Jiale Lin
(Corresponding author)
Department of Civil and Environmental Engineering
University of Illinois at Urbana-Champaign
205 N. Mathews Ave.
Urbana, IL 61801
(217) 333-7394
jiale2@Illinois.edu

and

Hyunil Jung
Department of Civil and Environmental Engineering
University of Illinois at Urbana-Champaign
205 N. Mathews Ave.
Urbana, IL 61801
(217) 333-7394
hyunilj2@Illinois.edu

**CGJ-2022-0608**
A paper **SUBMITTED** for Re-Review and possible publication in the *Canadian Geotechnical Journal*

July 2, 2023

**Abstract:**
A procedure is proposed to assess whether a liquefied strength should be applied to a zone of non-plastic silt, silty sand, and/or clean sand in a static or seismic stability analysis to assess the flow failure potential of dams and slopes. The procedure consists of the following five main steps to assess the flow failure potential: (1) assess static liquefaction potential of segments along a potential failure surface, (2) assess seismic liquefaction potential by calculating the factor of safety against liquefaction ($FoS_{Liquefaction}$) for any amplitude of shaking; (3) if liquefaction is not triggered in any of these segments, assess the magnitude of shear-induced pore-water pressures due to seismic or vibratory events of any amplitude; (4) assign a liquefied strength to zone(s) that experience seismic liquefaction, i.e., $FoS_{Liquefaction} < 1$ or significant pore-water pressure generation, i.e., total pore-water pressure ratio $\geq 0.7$; and (5) conduct a post-triggering stability analysis to assess flow failure potential. This procedure is illustrated using the 1971 seismic permanent deformations of Upper San Fernando Dam and 2015 Fundão tailings dam failure.

**Keywords:**

Liquefaction, Slopes, Earthquakes, Dams, Embankments, Shear strength, Post-liquefaction.

## INTRODUCTION

The 2015 Fundão and 2019 Feijão tailings dam failures generated a need to refine the three-step flow failure analysis procedure proposed by Olson and Stark (2003). The Olson and Stark (2003) three-step procedure involves conducting a: (1) liquefaction susceptibility analysis by determining whether the non-plastic soil along a potential failure surface behaves as contractive or dilative material; (2) liquefaction triggering analysis; and (3) post-triggering/flow failure stability analysis. Numerous investigators e.g., Sladen and Hewitt 1989; Ishihara 1993; Fear and Robertson 1995; Baziar and Dobry 1995; Olson and Stark 2003, have proposed contractive susceptibility boundary lines based on penetration resistance, i.e., soil density and effective confining stress, to separate contractive and dilative shear behavior. These contractive boundary lines have been used to decide whether a liquefied strength should be applied in a post-triggering stability analysis. In particular, if the penetration resistance plots to the left of the contractive/dilative boundary line, a liquefied strength is applied to the applicable segment of the failure surface. Conversely, if the soil condition plots to the right of the contractive/dilative boundary line, a liquefied strength is not applied to the segment because the soil is deemed to be dilative and not susceptible to a large increase in pore-water pressure and strength loss. However, the 2015 Fundão and 2019 Feijão tailings dam flow failures and other case histories indicate the Olson and Stark (2003) contractive susceptibility boundary is unconservative and is revised herein.

The three-step flow failure analysis procedure proposed by Olson and Stark (2003) is also expanded herein to discontinue the use of a contractive/dilative boundary line and rely on an estimate of the shear-induced pore-water pressures to determine whether a liquefied strength should be applied. The new flow failure assessment for dams, embankments, and slopes during or after seismic or dynamic loading of any amplitude consists of the following five main steps: (1) assess static liquefaction potential of segments along a potential failure surface, (2) assess seismic/dynamic liquefaction potential along a potential failure surface by calculating the factor of safety against liquefaction ($FoS_{Liquefaction}$), i.e., ratio of cyclic resistance ratio (CRR) to cyclic stress ratio (CSR); (3) if liquefaction is not triggered in any of these segments, i.e., $FoS_{Liquefaction} > 1$, assess the magnitude of shear-induced pore-water pressures due to small seismic or other vibratory events in each segment; (4) assign a liquefied strength to zone(s) that experience seismic liquefaction, i.e., $FoS_{Liquefaction} < 1$, or significant pore-water pressure generation, i.e., total (static plus dynamic) pore-water pressure ratio greater than or equal to 0.7; and (5) conduct a post-triggering/flow failure stability analysis to assess flow failure potential. Procedures for assigning a liquefied strength or liquefied strength ratio are also presented in this paper, emphasizing the importance of incorporating them in post-triggering stability analyses to determine flow failure potential.

Procedures are available for assessing the seismic triggering of liquefaction in level and sloping ground, e.g., Seed and Harder (1990), Harder and Boulanger (1997), Mesri (2007), and Boulanger and Idriss (2014). Seed and Harder (1990) propose adjustment factors, $K_\alpha$ and $K_\sigma$, to modify the level ground cyclic resistance ratio to account for a static shear stress and an effective overburden stress greater than 100 kPa, respectively. Despite being updated by Harder and Boulanger (1997) and Boulanger and Idriss (2014), the $K_\alpha$ adjustment factor exhibits a large uncertainty in its application. Consequently, the corrections are sometimes omitted on small and moderately sized projects with horizontal ground. Otherwise, $K_\alpha$ should be included to determine whether $K_\alpha$ makes the project site more liquefiable. For large projects, site-specific adjustment factors can be developed, e.g., Pillai and Stewart 1994; Hedien et al. 1998. This paper also presents a method to assess the triggering of liquefaction for dams, embankments, and slopes.

If liquefaction is predicted to trigger along a segment or segments of a potential failure surface, this paper presents a procedure for estimating a liquefied strength or liquefied strength ratio for this segment(s) to evaluate flow failure potential for any magnitude of ground motion. This is important because if a zone develops a liquefied strength condition, it has a large impact on static and dynamic stability and thus flow failure potential.

If liquefaction is not predicted to trigger due to small earthquakes, blasts, equipment vibrations, or other dynamic disturbances, the magnitude of shear-induced pore-water pressures should be estimated to determine if a liquefied strength or strength ratio should be applied. This analysis is based on available empirical and numerical methods for assessing shear-induced pore-water pressures in level or sloping ground using the FoS against liquefaction ($FoS_{Liquefaction}$ ). For example, the shear-induced pore-water pressures can be estimated empirically using $FoS_{Liquefaction}$ in level or sloping ground from empirical correlations or numerical methods. If the shear-induced pore-water pressures are empirically predicted to result in a significant reduction in effective stress and warrant the application of a liquefied strength, a numerical analysis of the pore-water pressure generation can be performed using various constitutive models, e.g., UBCSAND (Beaty and Byrne, 2011), PM4SILT (Boulanger and Ziotopoulou, 2018), to improve the understanding of pore-water pressure generation. The shear-induced pore-water pressures are used to determine if the effective stress condition of a segment shifts to the left of the critical state locus in (q–p) space, which indicates mobilization of a liquefied strength due to soil contraction. This procedure is illustrated herein using the 1971 seismically-induced permanent deformations of Upper San Fernando Dam and 2015 Fundão Tailings Dam failure below.

After assigning a liquefied strength to the appropriate segment(s) along a potential failure surface, limit equilibrium stability analyses should be conducted without a seismic coefficient to assess the potential for flow failure, i.e., $FoS_{Flow}$. If the resulting $FoS_{Flow}$ decreases to less than unity (1.0), flow failure is likely and remedial measures should be applied (Olson and Stark, 2003). If the resulting $FoS_{Flow}$ is between 1.1 and 1.3 and the project justifies it, a numerical analysis of the resulting permanent deformations should be performed (Olson and Stark, 2003). If the resulting $FoS_{Flow}$ is greater than 1.3, no action is required (Olson and Stark, 2003). The following sections present additional details on these five tasks for assessing the flow failure potential of dams, embankments, and slopes

## YIELD AND LIQUEFIED STRENGTHS

**Fig. 1** schematically represents the undrained behavior of saturated sandy soil subjected to static and dynamic shear stresses. The undrained yield shear strength [$s_u$(yield)] is defined as the static peak shear strength (see Point B in **Fig. 1(a)**) available during undrained loading (Terzaghi et al. 1996). Undrained strain softening or strength loss can be triggered by either static or dynamic loads that exceed $s_u$(yield).

Point A in **Fig. 1(a)** represents the pre-existing stress and strain conditions in a soil element. Point A could have been reached by drained, partially drained, or completely undrained loading during dam or embankment construction (Eckersley, 1990 and Sasitharan et al., 1993). During placement of the next fill lift or an external applied shear stress, the soil element moves from Point A to Point B, which is located on the undrained yield strength envelope (see Point B in **Fig. 1(b)**). This step assumes that the drainage boundaries and hydraulic conductivity of the element result in an undrained loading condition. The value of $s_u$(yield) is close to the average undrained shear strength because different shear modes are present along the potential failure surface. When the shear stress in this element exceeds $s_u$(yield) at Point B, the soil structure yields, i.e., tends to contract, and positive shear-induced pore-water pressures are generated causing a reduction in effective stress and undrained strength. If pore-water pressure generation is sufficient to trigger liquefaction, the soil element moves from Point B to Point C in **Fig. 1(a)**, i.e., mobilization of a liquefied shear strength. With continued strain or deformation, the soil moves from Point C to Point D in **Fig. 1(a)** with no further strength loss because it corresponds to the liquefied strength.

For cases of static loading, small earthquakes or other small vibrations, the shear stress mobilized in the zone of contractive soil immediately prior to failure is approximately equal to $s_u$(yield). An inverse limit-equilibrium stability analysis of the pre-failure geometry provides a reasonable estimate of $s_u$(yield) and yield strength ratio [$s_u$(yield)/ $\sigma'_{vo}$] mobilized within the zone of liquefaction. The yield strength ratio is defined as $s_u$(yield) divided by the pre-failure vertical effective stress [$s_u$(yield)/$\sigma'_{vo}$].

Point A’ in **Fig. 1(a)** represents the pre-existing stress and strain conditions in a soil element that is subsequently subjected to dynamic shear stress. Point A’ also could have been reached by drained or undrained loading, and the static shear stress carried by the element is greater than its liquefied shear strength (Point C). If the dynamic loading is small and the soil element still mobilizes a liquefied strength, Point A' could be close to Point A. When large dynamic loads are required to trigger liquefaction, Point A' will be a significant distance from Point A but the soil element can still mobilize a liquefied strength with a large loading, e.g., Mochi-Koshi Tailings Dams and M= 7.0 earthquake (Ishihara, 1984). During a significant seismic or dynamic loading, positive shear-induced pore-water pressures are generated, which cause shear strain or deformation and the stress condition moves from Point A' to Point E.

If Point A' is a significant distance from Point A, the dynamic loading may not be sufficient for the stress condition to move from Point A' to Point E and the soil does not undergo substantial strain and strength loss. There may be field processes that occur during earthquakes that cause the liquefied strength to be less than what might be produced from an undrained monotonic test, e.g., generation of water films, void ratio redistribution, overlying confining layer, and mixing of thin soil layers. Therefore, inverse analysis of flow failure case histories provides a better estimate of the liquefied strength because it includes some unknown field factors that are not incorporated in laboratory shear tests.

At Point E, the mobilized strength is less than $s_u$(yield) so this dynamic loading situation cannot be used to estimate mobilized $s_u$(yield). This is due to the dynamic loading causing some cyclic softening, so the dynamic loading does not have to exceed $s_u$(yield) to cause additional strain or deformation. With continued strain or deformation, the soil element undergoes additional strength loss and moves from Point E to Point C in **Fig. 1(a)**, i.e., mobilization of a liquefied shear strength. With continued strain or deformation, the soil moves from Point C to Point D with no further loss of strength.

The yield strength envelope in **Fig. 1(b)** is the same as the instability line in Jefferies and Been (2016). The soil must reach or pass the yield strength envelope to induce a liquefied strength condition. The yield strength ratio is nearly equivalent to the inclination of the yield strength envelope. There are multiple stress paths that can lead to exceeding the yield strength envelope, such as static load, seismic load, reduction of effective stress due to pore-water pressure generation, drilling pressures, and permanent deformations.

## STATIC LIQUEFACTION ANALYSIS

The first of the five steps in assessing the flow potential of dams and embankments, and slopes involves evaluating the potential for static liquefaction and whether a liquefied strength or liquefied strength ratio should be applied to a segment(s) along a potential failure surface. This differs from the approach in Olson and Stark (2003) in which the first step of the flow failure analysis is to determine if the soil is contractive or dilative not whether a zone(s) will mobilize a liquefied strength, which is a later step. This is key because if a zone(s) mobilizes a liquefied strength, a flow failure can occur directly or via a progressive failure mechanism so determining whether a liquefied strength condition will develop under static conditions is a new and important first step.

**Fig. 2** presents CPT-based static flow failure cases from Olson and Stark (2002) and other sources (see **Table 1**) using the pre-failure effective vertical stress ($\sigma'_{vo}$) and cone tip resistance ($q_c$) normalized to an effective vertical stress of 101 kPa ($q_{c1}$) using the following expression where m is equal to 0.5:

$$q_{c1} = q_c * C_N \tag{1}$$

$$C_N = \left(\frac{P_a}{\sigma'_{v0}}\right)^m \quad (2)$$

where $q_c$ is cone penetration resistance in MPa. $C_N$ is blowcount overburden stress correction factor. $P_a$ is the atmospheric pressure of 101 kPa, and m is a parameter that depends on the soil properties and relative density.

These data were used to develop the static liquefied strength boundary line in **Fig. 2** (see dashed green line) between $q_{c1}$ and static flow failure case histories. This static liquefied strength susceptibility boundary is proposed instead of the contractive/dilative boundary line (see solid blue line in **Fig. 2**) presented in Olson and Stark (2003) for static flow failure assessments. The static liquefied strength boundary plots to the left of the Olson and Stark (2003) contractive/dilative boundary because representative values of $q_{c1}$ in available static flow failure cases plot to the left of contractive/dilative line.

To evaluate the potential for static liquefaction, the potential failure surface is divided into segments based on material type and penetration resistance, e.g., zones of high and low penetration resistance. If the $q_{c1}$of a segment plots to the left of the liquefied strength boundary in **Fig. 2** (see dashed green line) or lower than 4 MPa, the segment is susceptible to static liquefaction and should be assigned a liquefied strength because static conditions, e.g., equipment vibrations, construction activities, high drilling pressures, etc., may be able to reduce the effective stress sufficiently to change the soil from a metastable state to a liquefied state.

The liquefied strength boundary in **Fig. 2** was developed using available static liquefaction flow failure cases that do not involve seismic or vibratory loading. The static case histories plot at or to the left of the proposed liquefied strength boundary line (see dashed green line), which can be used as an initial screening tool for digitized $q_{c1}$ data in a spreadsheet.

**Table 1** presents the static flow failure case histories used to create **Fig. 2** including a weighted average pre-failure vertical effective stress and three values of $q_{c1}$. In particular, **Table 1** presents values of $q_{c1}$ that correspond to the best estimate (BE), upper bound (UB), and lower bound (LB) values of $q_{c1}$ based on the reported penetration data. This range in $q_{c1}$ is used to plot the error bars in **Fig. 2**.

Fines content correction is suggested to be used for experienced engineer when the fines content is available. The following discusses the calculation procedure for m and normalization of the cone tip resistance to a clean sand ($q_{c1N\text{-}cs}$) presented by Idriss and Boulanger (2009):

$$m = 1.338 - 0.249(q_{c1N})^{0.264} \qquad (3)$$

The equation above for "m" is available when $q_{c1N}$ is limited to values between 21 and 254 atm in Boulanger and Idriss (2009). The value of $q_{c1N}$ is $q_{c1}$ normalized by atmospheric pressure (101 kPa) as shown below by Roberson and Wride (1998) using the following equation:

$$q_{c1N} = \frac{q_{c1}}{P_a} \qquad (4)$$

**Table 2** presents the static flow failure case histories in **Table 1** with a fines content correction that are used to create **Fig. 3**. The best estimate values of $q_{c1}$ in **Table 1** is used to calculate the clean sand normalized cone penetration resistance ($q_{c1N-cs}$) using the following fines content, i.e., percent passing No. 200 sieve, correction:

$$\mathrm{q}_{\mathrm{c1N-cs}} = q_{c1N} + \Delta q_{c1N} \tag{5}$$

where the fines adjustment factor, $\Delta q_{c1N}$, is a function of the fines content (FC) as shown below:

$$\Delta q_{c1N} = \left(11.9 + \frac{q_{c1N}}{14.6}\right) \exp\left(1.63 - \frac{9.7}{FC+2} - \left(\frac{15.7}{FC+2}\right)^2\right) \tag{6}$$

**Fig. 3** presents CPT based static flow failures using the $\sigma'_{vo}$ and $q_{c1N-cs}$. The proposed average static liquefied strength susceptibility boundary in **Fig. 3** can be modeled using the following expression:

$$\sigma'_v = 0.02 \times {q_{c1N-cs}}^2 + 0.2715 \times q_{c1N-cs} - 28 \tag{7}$$

If $q_{c1N-cs}$ plots to the left of the liquefied strength boundary line (see dashed dark green line in **Fig. 3**), the zone has a potential to undergo static liquefaction. Therefore, these segments should be assigned a liquefied strength because equipment vibration, construction activities, high drilling pressures, etc. may be able to reduce the effective stress sufficiently to change the soil from a metastable state to a liquefied state. If the soil plots to the right of the dashed green line, it initially can be considered non-liquefiable, but the designer should proceed to Step #2 of the five-step flow failure procedure.

The use of three values of $q_{c1}$ in **Table 1** allows a range of penetration resistance to be used in developing the boundary lines shown in **Fig. 4**. **Table 3** presents data for the flow failure case histories analyzed by Olson and Stark (2003) with a weighted average $\sigma'_{vo}$ and $q_{c1}$ that were used to create **Fig. 4**. **Table 4** and **Table 5** present data for additional flow failure case histories analyzed herein and analyzed by Muhamad (2012), which are included in **Fig. 4**. In particular, **Fig. 4** presents the static liquefied strength boundary from **Fig. *2***, Olson and Stark (2003) contractive/dilative boundary, and a new seismic liquefied strength boundary. For comparison purposes, **Fig. 4** also presents the contractive/dilative boundaries proposed by Sladen and Hewitt (1989) and Robertson (2010).

**Table 6** summarizes all of the data used to develop the correlation between peak ground acceleration (PGA), $q_{c1N\text{-}cs}$, and effective normal stress shown in **Fig. 5**. The effective vertical stress ($\sigma'_v$) and liquefied strength in **Table 6** are from Weber (2015) and update the values of liquefied strength presented in **Table 3** as discussed in Step # 4 of the flow failure procedure below. Therefore, the case histories summarized in these six tables present the entire database used herein to develop the flow failure assessment procedure for dams, embankments, and slopes so readers can review the cases.

## LIQUEFACTION TRIGGERING ANALYSIS

The second of the five steps in assessing the flow potential of dams, embankments, and slopes involves performing a liquefaction triggering analysis to determine if a liquefied strength should be applied to a segment(s) of the potential failure surface due to ground shaking. An inverse analysis of thirty-eight liquefaction flow failures, i.e., thirty-one case histories presented in Olson and Stark (2003) and seven case histories analyzed herein, was conducted to relate $q_{c1}$ to field situations where a liquefied strength was mobilized due to ground shaking. Static and low-level shaking flow failures are included because Points A and A’ in **Fig. 1** can be close together. As a result, the yield strength and yield strength ratio obtained for an inverse analysis using the pre-failure geometry corresponds to the yield strength envelope.

**Fig. 4** presents boundary lines between $q_{c1}$ and static or seismic flow failure case histories. This plot presents a seismic liquefied strength susceptibility boundary (see solid black line) that is to the right of the static liquefied strength boundary presented in **Fig. 2** as a dashed green line and to the right of the contractive/dilative boundary line (see solid blue line) from Olson and Stark (2003). Recent case histories plotted in **Fig. 4** again show the contractive/dilative boundary line in Olson and Stark (2003) is unconservative. The contractive/dilative boundary was drawn primarily using the mean values of $q_{c1}$ for a given case history instead of the upper bound of the data range. As a result, some of the recent case histories plot to the right of the contractive/dilative boundary line now making it unconservative.

The proposed liquefied strength susceptibility boundary (see solid black line in **Fig. 4**) represents the upper bound of current flow case histories and adequately explains recent flow failures. As additional case histories become available, the proposed seismic and static liquefied strength susceptibility boundaries in **Fig. 4** will be adjusted to ensure a conservative approach because of the large consequences of a flow failure. The proposed seismic liquefied strength susceptibility boundary in **Fig. 4** can be modeled using the following expression:

$$\sigma_v' = 3.01 \times 10^{-7} \times {q_{c1}}^{8.796} \tag{8}$$

where $\sigma_v'$ and $q_{c1}$ have units of kPa and MPa, respectively.

This paragraph uses the Fundão tailings dam failure to demonstrate this step of the flow potential assessment procedure, which is described in detail by Stark et al. (2023). The plateau area in the left abutment setback of the Fundão tailings dam was estimated not to mobilize a liquefied strength based on site response analyses and available $q_{c1}$ data by Stark et al. (2023) because it plots outside the new boundary (see open blue square data point in **Fig. 4**). If the shaking induced by the three earthquakes that occurred in the left abutment of Fundão tailings dam on the day of failure were stronger, the plateau in the left abutment setback might have developed sufficient shear-induced pore-water pressures to mobilize a liquefied strength because the open blue square data point plots just outside of the seismic liquefied strength susceptibility boundary in **Fig. 4**. Conversely, the left abutment downstream slope and toe areas plot inside the new boundary (see open green diamond and open light blue triangle data points in **Fig. 4**) so these two areas were assigned a liquefied strength based on site response analyses and available $q_{c1}$ data by Stark et al. (2023) in the post-triggering stability analysis.

Some other researchers (Boulanger and Idriss, 2014; Poulsen et al, 2012, 2013) have shown excess pore-water pressure generation can occur even when the cone tip resistance is greater than 9 MPa. For example, Poulsen et al. (2012, 2013) show that a total cone tip resistance ($q_t$) of 9 MPa at depths from 4.5 to 11 m can still generate positive excess pore-water pressure that can lead to mobilization of a liquefied strength condition. The value of $q_t$ is calculated by subtracting the pre-failure total vertical stress ($\sigma_{vo}$) from $q_c$ or $q_t = q_c - \sigma_{vo}$.

Many cases with $q_{c1}$ of 12 MPa or greater from Boulanger and Idriss (2014) liquefied during large ground motions. As a result, significant pore-water pressures may still be generated at field conditions that plot to the right of the boundary line because Boulanger and Idriss (2014) show a $q_{c1}$ greater than 15 MPa is, i.e., $q_{c1N\text{-}cs}$~160, required before liquefaction is not triggered by seismic loading.

Robertson (2010) also suggests a liquefied strength boundary based on a normalized total cone penetration parameter with fine content correction ($Q_{tn,cs}$). Robertson (2010) suggests $Q_{tn,cs} \leq 70$ as the boundary between assigning liquefied and non-liquefied strengths. However, Robertson (2010) also mentions there are several flow failures in Olson and Stark (2003) that show $Q_{tn,cs}$ greater than 70. As a result, Robertson (2021) suggests tailings sand with bonding can liquefy with $Q_{tn,cs}$ greater than 70. The value of $Q_{tn,cs} = 70$ was converted to $q_{c1}$ using a soil behavior index of $I_c = 1.64$ because the empirical correlation in Olson and Stark (2003) uses $q_{c1}$. The values of $q_{c1}$ were calculated using $Q_{tn,cs} = 70$ and different values of $\sigma'_{vo}$ and they plot to the right of the Olson and Stark (2003) contractive/dilative boundary line but considerably to the left of the proposed liquefied strength boundary line (see solid black line in **Fig. 4**). More importantly, some of the flow failure cases in **Fig. 4** plot near the $q_{c1}$ boundary line (see black solid line) so this boundary may not capture all future cases but it captures more field case histories than the contractive/dilative boundary proposed by Olson and Stark (2003).

After $q_{c1}$ is corrected for fines content (% passing No. 200 sieve), the proposed liquefied strength susceptibility boundary represents the mean $q_{c1N\text{-}cs}$ value from current flow case histories at different levels of shaking and is shown in **Fig. 5**. The square (magenta) data points correspond to the static flow failure case shown in **Fig. 4**, while the dots, diamonds, and open circle data points correspond to the flow failure cases at PGA $\leq$ 0.2g , 0.2 < PGA $\leq$0.4g and PGA $\geq$ 0.4g, respectively.

**Fig. 5** shows as the PGA increases, some soil with high values of $q_{c1N\text{-}cs}$ can still experience flow failure. The dashed red line in **Fig. 5** represents the probability of liquefaction occurring when PGA $\leq$ 0.2g. The dash-dot blue line shows a possible liquefiable triggering line at medium shaking level (0.2g < PGA $\leq$ 0.4g). The three short and long dashed green line is a liquefiable triggering line at high ground shaking (0.4g < PGA). For comparison purposes, **Fig. 5** also presents the static liquefaction boundary from **Fig. 4** (see dashed green line). A data point plotting to the left of one of the potential liquefiable or liquefied strength trend lines has a high probability of mobilizing a liquefied strength. A data point plotting to the right side of one of the potential liquefiable or liquefied strength trend lines has a low probability of mobilizing a liquefied strength but could still liquefy if a ground motion stronger than the associated PGA impacts the site. Some uncertainties also might shift the boundary line to the right, such as, a higher shaking level, high initial shear stress in slope, soil with uniform gradation, etc. Therefore, there is no defined $q_{c1N\text{-}cs}$ threshold beyond which no flow failure could/would occur under seismic/dynamic loading.

Engineers should consider the local ground motion level to design the structure. However, some of the segments along the observed failure surface in the case histories used in **Fig. 5** may have experienced localized liquefaction and mobilization of liquefied strength but did not experience global or flow failure. For example, segments along a sloped area with a low density have a higher static shear stress ratio, which are more susceptible to liquefaction and/or mobilizing a liquefied strength ratio under low shaking. Conversely, there are segments near the base of the dam or embankment that are subjected to high normal stresses and may experience some horizontal displacement but not liquefication and/or mobilization of a liquefied strength even under a seismic event. In other words, there may be localized deformations or pore-water pressure generation but not liquefaction or mobilization of a liquefied strength over a large area such that global flow failure does not occur.

**Fig. 4** and **Fig. 5** provide an update of contractive/dilative boundary proposed by Olson and Stark (2003), which has been widely adopted by engineers and practitioners. The liquefaction triggering analysis should be performed following the procedure of Boulanger and Idriss (2014) to estimate the $FoS_{Liquefaction}$, i.e., CRR divided by the CSR. If liquefaction is triggered in a soil segment along a potential failure surface, i.e., $FoS_{Liquefaction}$ is less than unity (1.0), a liquefied shear strength should be applied to that segment. The $FoS_{Liquefaction}$ is also used in Step #3 of the proposed five-step flow failure procedure to estimate the magnitude of shear-induced pore-water pressures generated if liquefaction is not triggered in Step #2 so $FoS_{Liquefaction}$ need to be calculated at this point in the five-step procedure.

The $FoS_{Liquefaction}$ is calculated by following the method proposed by Boulanger and Idriss (2014). The CSR computed for a specific earthquake magnitude (moment magnitude, M) and $\sigma_v'$, $CSR_{M,\sigma_v'}$, is estimated using the maximum horizontal shear stress, $\tau_{h,max}$, obtained from a site response analysis as outlined by Idriss and Boulanger (2008) or from ground surface accelerations:

$$CSR_M = 0.65 * \frac{\tau_{\max}}{\sigma_{vc}^{'}} = 0.65 * a_{\max} * \frac{\sigma_{vc}}{\sigma_{vc}^{'}} * r_d \tag{9}$$

where $a_{max}$ is the maximum ground surface acceleration, and $r_d$ is a shear stress reduction coefficient as outlined by Idriss and Boulanger (2008). If the bedrock ground motion is used, a site response analysis should be performed to estimate the value of $\tau_{h,max}$. at a particular depth.

Boulanger and Idriss (2014) shows $FoS_{Liq}$ can be estimated for sloping ground using the following expression:

$$FoS_{Liquefaction} = \frac{CRR_{M,\sigma_v'}}{CSR_{M,\,\sigma_v'}} = \frac{CRR_{M=7.5,\sigma_v'=1atm} \times MSF \times K_\sigma \times K_\alpha}{CSR_{M,\,\sigma_v'}} \tag{10}$$

Where, $CRR_{M=7.5,\sigma_v'=1atm}$ is the CRR values adjusted to a reference M = 7.5 and $\sigma_v'$ = 1 atm and expressed as a function of $q_{c1N-cs}$:

$$CRR_{M=7.5,\sigma_v'=1atm} = \exp\left(\frac{q_{c1N-cs}}{113} + \left(\frac{q_{c1N-cs}}{1000}\right)^2 - \left(\frac{q_{c1N-cs}}{140}\right)^3 + \left(\frac{q_{c1N-cs}}{137}\right)^4 - 2.8\right) \tag{11}$$

MSF is the earthquake magnitude scaling factor, $K_\sigma$ is the overburden stress adjustment factor, and $K_\alpha$ is the sloping ground adjustment factor. Detailed explanation of these factors is provided in Boulanger and Idriss (2014).

## PORE-WATER PRESSURE GENERATION ANALYSIS

The third of the five steps in assessing the flow potential of dams, embankments, and slopes involves calculating the magnitude of shear-induced pore-water pressures generated, if liquefaction is not triggered in Step #2. This step was added based on the analysis of the three earthquakes that occurred shortly before the Fundão tailings dam flow failure and one earthquake before the Palu flow failure (Hidayat et al., 2020 and Mason et al., 2021). The following paragraphs describe how to estimate the shear-induced pore-water pressures, which are used to determine if a liquefied strength is mobilized and if not, the pore-water pressures are included in the post-triggering analysis. If the shear-induced pore-water pressures are sufficient to move the stress conditions to the left of the critical state locus in (q–p) space, a liquefied strength is applied to that segment(s) of the potential failure surface in the post-triggering stability analysis.

The shear strength of a soil is expressed using the following expression:

$$\tau = c' + (\sigma_v - u)*\tan(\phi') = c' + (\sigma'_v)*\tan(\phi') \tag{13}$$

where $\tau$ is the soil shear strength mobilized on the failure surface, c' is effective stress cohesion, $\sigma_v$ is the pre-failure total vertical stress, i.e., $\gamma_{soil}*h_{soil}$, $\gamma_{soil}$ is the saturated soil unit weight below the groundwater level and total unit weight above the groundwater level, $h_{soil}$ is the depth below the ground surface for each unit weight, u is the sum of hydrostatic and shear induced pore-water pressure, $\sigma'_v$ is the effective vertical stress, and $\phi'$ is the effective stress friction angle of the embankment material.

The value of total excess pore-water pressure, i.e., hydrostatic plus dynamic, should be used to estimate $\sigma'_v$ in the post-triggering/flow failure analyses described below. Therefore, shear-induced pore-water pressures and the corresponding value of $\sigma'_v$ has a large influence on the shear strength of materials along a potential failure surface even if the segment does not liquefy. This explains why the generation of pore-water pressures during an earthquake, other vibratory events, or drilling pressures are important to overall stability because the higher the pore-water pressure ratio, i.e., the lower $\sigma'_v$, the more likely a liquefied strength condition can develop.

Using the liquefaction assessment procedure in Boulanger and Idriss (2014), the $FoS_{Liquefaction}$ is calculated and then used to estimate the shear-induced pore-water pressures. In general, if the $FoS_{Liquefaction}$ is less than 2.5, excess pore-water pressures can be generated in loose, saturated cohesionless materials, e.g., loose non-plastic silt, silty sand, clean sands and/or sandy tailings. Values of $FoS_{Liquefaction}$ can be used to estimate the level of excess pore-water pressure induced by each earthquake or vibratory event using the $FoS_{Liquefaction}$ and sand relationships shown in **Fig. 6**. The resulting values of seismic pore-water pressure ratio, $r_{u,seismic}$, correspond to:

$$r_{u,seismic} = \left(\frac{u_{dynamic}}{\sigma'_{v0}}\right) \tag{14}$$

where $u_{dynamic}$ is the excess pore-water pressure induced by shaking or other vibratory event and $\sigma'_{v0}$ is the initial effective vertical stress before shaking (Marcuson et al., 1990). Therefore, the definition of $r_{u,seismic}$ is slightly different than the hydrostatic pore-water pressure ratio, which is:

$$r_{u,static} = \left(\frac{u_{static}}{\sigma_v}\right) \quad (15)$$

where $u_{static}$ is the hydrostatic pore-water pressure and $\sigma_v$ is total vertical stress, i.e., $\gamma_{soil}$*$h_{soil}$, of the overlying soill before shaking not $\sigma'_{v0}$. As a result, $r_{u,seismic}$ has to be converted to the hydrostatic framework to be added to $r_{u,static}$ to calculate the total pore-water pressure ratio, $r_{u,total}$ for estimating the effective vertical stress after the dynamic event. Converting $r_{u,seismic}$ to $r_{u,static}$ also facilitates the use of $r_{u,total}$ in post-triggering stability analyses because existing limit equilibrium slope stability software utilizes $r_{u,static}$ not $r_{u,seismic}$.

$$r_{u,static} = r_{u,seismic} \times \frac{\sigma'_{v0}}{\sigma_{v0}} \quad (16)$$

The shear-induced pore-water pressure relationships shown in **Fig. 6** were derived from Tokimatsu and Yoshimi (1983), Seed et al. (1976), and Marcuson et al. (1990). The upper bound of the Tokimatsu and Yoshimi (1983) relationship is shown in **Fig. 6** and is significantly higher than the sand upper bound from Marcuson et al. (1990) because Marcuson et al.(1990) measured the pore-water pressure after shaking not during shaking. The upper bound Tokimatsu and Yoshimi (1983) relationship was derived using the following expression:

$$r_{u,seismic} = 0.5 + \frac{sin^{-1}\left(2*F_{Liq}^{\frac{1}{\alpha\beta}} - 1\right)}{\pi} \quad (17)$$

where representative values of $\alpha$ and $\beta$ are unity (1) and -0.1 to -0.5, respectively. **Fig. 6** shows the relationships for $\alpha$ of unity (1) and $\beta$ of -0.5 and -0.3 both of which exceed the Marcuson et al.

(1990) range. Seed et al. (1976) present a similar relationship for $r_{u,seismic}$, which is shown below:

$$r_{u,seismic} = 0.5 + sin^{-1}(2 * r_N^{\frac{1}{\alpha}} - 1)/\pi \tag{18}$$

where $r_N$ is the ratio of the number of earthquake cycles to cause a pore-water pressure ratio of unity (1.0), i.e., liquefaction, and $\alpha$ is an empirical constant with a value around unity. The importance of this discussion is the sand relationship proposed by Marcuson et al. (1990) were derived from established relationships and are in better agreement with the Tokimatsu and Yoshimi (1983) relationships. The relationships shown in **Fig. 6** also may be applicable to other dynamic sources, such as, equipment vibrations, construction activities, drilling, and blasting, for estimating shear-induced pore-water pressures and thus are recommended herein.

The dataset used by Tokimatsu and Yoshimi (1983) to develop their relationships in **Fig. 6** include water retaining structures and tailings dams so it is reasonable to apply it to similar structures. In summary, the upper bound of the Marcuson et al. (1990) sand relationship in **Fig. 6** is close to $\beta$ = -0.2 in the Tokimatsu and Yoshimi (1983) correlation and the lower bound of the Marcuson et al. (1990) is close to $\beta$ = -0.1 in the Tokimatsu and Yoshimi (1983) correlation. The value of $\beta$ for most soils is between -0.5 and -0.1 in Tokimatsu and Yoshimi (1983). Therefore, the upper bound Marcuson et al. (1990) relationship in **Fig. 6** is recommended to assess the value of $r_{u,seismic}$ for zones that do not trigger liquefaction in Step #2 of the five steps flow failure procedure. The resulting shear-induced pore-water pressures are used to estimate the effective vertical stress along a segment of a potential failure surface. If possible, these shear-induced pore-water pressures should be confirmed by numerical methods that have constitutive models that can estimate pore-water pressure generation due to small to medium shaking/vibratory events.

## ASSIGNING LIQUEFIED AND YIELD STRENGTHS

The fourth of the five steps in assessing the flow potential of dams, embankments, and slopes involves assigning a liquefied strength to failure surface segment(s) that trigger liquefaction or significant pore-water pressure generation. Therefore, it should not be assumed that an unknown trigger will occur the liquefaction and segments of the potential failure surface should be automatically assigned a liquefied shear strength for a post-triggering/flow failure stability analysis. In other words, it is not necessary to evaluate the stability of the structure using liquefied shear strengths after assuming the soil is liquefied by an unknown trigger. This is important because a liquefied strength is about one-third of the peak undrained strength, which means applying a liquefied strength results in a post-triggering or flow factor of safety ($FoS_{Flow}$) significantly below the triggering factory of safety ($FoS_{Triggering}$). If engineers were to design assuming an unknown trigger, it would result in values of $FoS_{Flow}$ well below unity in many, if not all, existing upstream raised tailings dam even though they are still stable. In other words, assuming an unknown trigger would require retrofitting thousands of upstream raised tailings dam and most likely many centerlines raised tailings dam even though they are stable.

Stark et al. (2012) shows the $r_{u,seismic}$ relationship from 0.7 to 1.0 in **Fig. 6** is nearly vertical at the same $FoS_{Liquefaction}$, which resulted in selecting a value of $r_{u,total}$ of 0.7 being the criterion for applying a liquefied strength. Segments along the potential failure surface that: (1) are identified as susceptible to static liquefaction using **Fig. 2**, (2) exhibit a $FoS_{Liquefaction} \leq$ unity (1.0), (3) experience an $r_{u,total}$ large enough to reduce the average effective normal stress of the area to the critical state locus in (q–p) space, and/or (4) have a value of $r_{u,total}$ greater than or equal to 0.7 based on Stark et al. (2012) should be assigned a liquefied strength or liquefied strength ratio.

**Fig. 7** shows the relationship between the liquefied strength ratio and $q_{c1}$ without fines content correction and **Fig. 8** shows the relationship between the liquefied strength ratio and $q_{c1N\text{-}cs}$ with fines content correction. When the fines content is available, **Fig. 8** is suggested to be used for experienced engineer. The values of $q_{c1}$, $q_{c1N\text{-}cs}$, effective normal stress, and undrained liquefied strength ($S_{u,Liq}$) used to develop correlations in **Fig. 7** and **Fig. 8** are summarized in **Table 6**. The following expression can be used to represent the average trend line in **Fig. 7**, which includes a wider range of $q_{c1}$ than a similar relationship in Olson and Stark (2003).

$$\frac{S_u\ (LIQ)}{\sigma_v'} = 0.03 + 0.0143\ (q_{c1}) \pm 0.03, q_{c1} < 10\ MPa \qquad (19)$$

The effective vertical stress $\sigma_v'$ in Eqn. (19) is the pre-failure effective vertical stress without including the excess or shear-induced pore water pressures from vibratory events. The trend line from Robertson (2010) in **Fig. 7** shows a quicker increase in liquefied strength ratio for values of $q_{c1}$ greater than 5 MPa than the average trend line, which could overpredict the liquefied shear strength. Additional case histories collected by Hazarika et al. (2020) fall within the upper and lower boundaries proposed by Olson and Stark (2002) and are shown in **Fig. 7**.

The liquefied strength ratio can be also assessed using equations proposed by Idriss and Boulanger (2015) with an upper bound of drained shear strength ratio, i.e., $\tan\phi'$. For the case where void redistribution is expected to be significant, the relationship can be approximated as follows (see black dashed line in **Fig. 8**):

$$\frac{S_u\ (LIQ)}{\sigma_v'} = \exp\left(\frac{q_{c1N-cs}}{24.5} - \left(\frac{q_{c1N-cs}}{61.7}\right)^2 + \left(\frac{q_{c1N-cs}}{106}\right)^3 - 4.42\right) \leq \tan\phi' \tag{20}$$

For the case where void redistribution is expected to be negligible, the relationship can be approximated as follows (see red dashed line in **Fig. 8**):

$$\frac{S_u\ (LIQ)}{\sigma_v'} = \exp\ (\frac{q_{c1N-cs}}{24.5} - \left(\frac{q_{c1N-cs}}{61.7}\right)^2 + \left(\frac{q_{c1N-cs}}{106}\right)^3 - 4.42) \times (1 + \exp\left(\frac{q_{c1N-cs}}{11.1} - 9.82\right)) \leq \tan\phi' \tag{21}$$

Segments along the potential failure surface that are not assigned liquefied strengths should be assigned a yield strength ratio using **Fig. 9** in the post-triggering stability analysis. It should be noted that the value of effective normal stress for the yield strength ratio should be determined by subtracting the estimated shear-induced pore water pressures in step #3 from the initial condition. Only the static case histories from Olson and Stark (2003) and Muhammad (2012) were reanalyzed herein to estimate the mobilized yield strength and yield strength ratio. This is to exclude the effect of cyclic softening caused by dynamic loading. This reanalysis shows the Olson and Stark (2003) upper and lower bound trend lines for yield strength are in agreement with the field case histories analyzed herein and are shown in **Fig. 9**. Detailed explanation for how the mobilized yield strength and yield strength ratio were estimated is provided in Olson and Stark (2003) and Muhammad (2012).

## POST-TRIGGERING STABILITY ANALYSIS

The fifth and final of the five steps in assessing the flow potential of dams, embankments, and slopes involves conducting a post-triggering/flow failure stability analysis. The post-triggering stability analysis must analyze noncircular and/or compound failure surfaces, i.e., not circular failure surfaces, that vary considerably in depth and location within the segment(s) of liquefiable soil and/or soil that will generate significant shear- or drilling-induced pore-water pressures. If the noncircular and/or compound failure surfaces cross segment(s) of soil that will generate significant pore-water pressures and/or liquefy at about the same location and depth, it is recommended that one or two additional potential failure surfaces that cross these soils at different depths be analyzed to locate the critical failure surface.

If the $FoS_{Liquefaction}$ <1 or $r_{u,total} \geq 0.7$ in a segment of a potential failure surface, the corresponding segment should be assigned a liquefied strength. If $FoS_{Liquefaction}$ is between 1.0 and 1.1 or $r_{u,total}$ < 0.7, the segment should be assigned with a yield strength or drained friction angle with the generated shear-induced pore water pressure. With these segments assigned a liquefied strength or drained strength with the shear-induced pore water pressures, the FoS against flow failure ($FoS_{Flow}$), which is total shear resistance/total driving force, should be calculated.

The $FoS_{Flow}$ assessment criteria follow the recommendations in Olson and Stark (2003). If the $FoS_{Flow}$ is between unity and about 1.1, some deformation is likely, and segments of the failure surface with marginal values of $FoS_{Liquefaction}$, i.e., less than about 1.1, should be assigned a liquefied shear strength due to the potential for additional shear deformation. The post-triggering stability analysis should be repeated with the marginal segment(s) being assigned a liquefied shear strength to determine a new $FoS_{Flow}$. This accounts for the potential of deformation-induced liquefaction and progressive failure of the structure in segments with $FoS_{Liquefaction}$, i.e., less than or about 1.1. The minimum $FoS_{Flow}$ will be calculated when liquefaction is triggered in all segments that can generate significant pore-water pressures and are assigned liquefied shear strengths at step #4 for the flow failure stability analysis. This condition can be analyzed to determine the worst-case value of $FoS_{Flow}$ in terms of post-triggering stability analysis and to aid judgments regarding the need for redesign or remediation. In general, if the $FoS_{Liquefaction}$ is below 1.2 to 1.3, applying a liquefied strength to segments of a potential failure surface will usually result in a significant reduction in $FoS_{Flow}$. If the $FoS_{Flow}$ is between 1.1 and 1.3, calculate permanent deformations using empirical or numerical methods and assess whether they are tolerable. If the $FoS_{Flow}$ is greater than 1.3, no action is required. These criteria are considered reasonable for the evaluation of many liquefaction cases, but further consideration may be needed for large or high consequence structures.

## UNCERTAINTY IN APPLYING THE SUGGESTED PROCEDURE

This section discusses the uncertainty associated with applying the new five-step flow failure assessment procedure. The uncertainty in this procedure comes mainly from the following six sources: (1) poor measurement of cone penetration tip resistance due to equipment or calibration issues; (2) some of the cone penetration tip resistance values were derived from standard penetration test blow counts using the conversion in Stark and Olson (1995); (3) delineating zones of potential liquefaction; (4) variation of noncircular and compound failure surfaces through the liquefied zone;

(5) shear strength of non-liquefied soil along the potential failure surface; and (6) uncertainty related to the location of the phreatic surface and soil unit weights.

For **Fig. 2** and **Fig. 3**, chemical bonding within the tailings dam material can induce a high measurement of cone tip resistance data (Robertson, 2010, 2021) but the material can still liquefy with sufficient external loading or human activity on the dam . The liquefied soil propagation zone and spatial uncertainty are not fully quantified herein because of the sparse amount of cone penetration test data available in most of the field case histories. To reduce some of the uncertainties mentioned above, more cone penetration data should be obtained to better define the liquefied zone and remediation methods suggested to reduce the flow failure potential of the dam.

For **Fig. 4** and **Fig. 5**, intense ground motion could cause significant seismic shear stress or generate significant pore water pressure which might cause some data points to plot outside of the current upper bound of the liquefied strength boundary. Variations in the reduction of liquefied strength at the bases or toes of failure surfaces that enter bodies of water or that travel outward into areas occupied by weak sediments contribute to analysis uncertainties. The assigned liquefied strength also has some uncertainty in **Fig. 7** and **Fig. 8** because some cases show a liquefied strength that is outside the current suggested boundary line (see black dashed circles in the bottom right of **Fig. 7** and **Fig. 8**).

The converted CPT data from SPT blow counts using the conversion in Stark and Olson (1995) also induces some uncertainty. Many case histories included in this study only have SPT data available and thus were converted to CPT data. The proposed conversion method shows agreement with measured data but some of the cases show the converted CPT data have more than a 10% difference from the measured data. The uncertainty within this CPT data might cause an increment of uncertainty in the liquefied strength boundary used in **Fig. 2**, **Fig. 3**, **Fig. 4**, and **Fig. 5**. As a result, the predicted liquefied strength may have a 10% or more difference in **Fig. 7** and **Fig. 8** due to the conversion of SPT data to CPT tip resistance.

The phreatic surface and the failure surface passing through the liquefied material is defined based on engineering judgment to simulate the actual post-failure slope surface in various inverse analyses. For example, Olson and Stark (2003), Muhammad (2012), and Weber (2015) use slightly different failure surfaces in some case histories which induces some uncertainty in the resulting empirical correlation. The typical unit weight of soil varies less than 10% from the measured data but also introduces additional uncertainty into the analysis.

To quantify this uncertainty, Duncan (2000) proposes a method to calculate the probability of failure ($P_f$) and/or the reliability of the computed FoS based on the Most likely Values (MLV) of the design input parameters. The main uncertainty in the new flow failure assessment procedure comes from the six different design input parameters described above. Therefore, for each of these input parameters, values of standard deviation (σ) and its corresponding FoS should be calculated to estimate $P_f$ for a specific slope as outlined by Idries and Stark (2024). Nevertheless, the quantification of the uncertainty in design input parameters for the new flow failure assessment procedure is outside the scope of this paper but is the topic of a future publication.

## EXAMPLE #1 – UPPER SAN FERNANDO DAM

This section demonstrates application of the five steps procedure for assessing the flow potential of dams, embankments, and slopes described above using the liquefaction-induced permanent deformations of Upper San Fernando Dam (USFD) during the 1971 San Fernando earthquake. On February 9, 1971, the San Fernando earthquake ($M_w$=6.1) with a peak acceleration of 0.55g to 0.60g caused USFD in the San Fernando Valley, California to experience small to moderate downstream liquefaction-induced deformations. The USFD case history is used because the localized liquefaction and/or pore-water pressure generation did not result in a flow failure, so this assessment is somewhat of a forward analysis, instead of an inverse analysis of a flow failure, to illustrate the application of this flow failure procedure.

This assessment focuses on pore-water pressure generation during the 1971 earthquake that occurred shortly before the observed permanent deformations. The recorded increases in piezometric level due to the earthquake shaking are shown in **Fig. 10**. These piezometer data were used to locate the phreatic surface before the earthquake and provide an estimate of the hydrostatic and earthquake-induced pore-water pressures for the flow failure assessment. As **Fig. 10** shows a substantial amount of excess pore-water pressure was generated especially in the upstream hydraulic fill (Zone P1) and the core area of the dam (Zone P2) such that water overflowed from the top of these piezometers (Serff et al., 1976). The location of these three piezometers (P1, P2, and P3) are shown in **Fig. 11.** The piezometric level in P1 suggests liquefaction of the upstream hydraulic sand fill. The measured excess pore pressure ratio of the downstream hydraulic sand fill (P3) after the earthquake is shown in **Table 7**.

**Fig. 11** presents cross-section B-B' of USFD located near the center of USFD from Chowdhury et al. (2018). The estimated failure surface based on field observations and numerical analyses (see dashed red line in **Fig. 11**) extends from the upstream hydraulic fill sand, downward through the clay core, and exits at the downstream toe area (Beaty and Byme, 2001 and Chowdhury et al., 2018). This failure surface is divided into five segments or zones (see **Fig. 11**) so values of $FoS_{Liquefaction}$ for each zone can be calculated using nearby pre-failure Standard Penetration Test (SPT) results.

The $FoS_{Liquefaction}$ was calculated for loose hydraulic sand fill zones of the dam using the liquefaction triggering procedure in Boulanger and Idriss(2014). **Table 7** shows the representative $N_{1,60\text{-}cs}$ due to the absence of pre-failure CPT data for each segment selected from **Fig. 12**, as well as the calculated $FoS_{Liquefaction}$. The magnitude of shear-induced pore-water pressure generated during the ground motion was calculated to determine whether the soil mobilized a yield or liquefied strength. The $FoS_{Liquefaction}$ for segments #1, #2, and #4 are less than unity, and thus a liquefied strength was applied to these segments. However, segment #5 was determined to not mobilize a liquefied strength because the $FoS_{Liquefaction}$ is greater than unity, i.e., 1.3, and the stress condition did not move to the left of the critical state locus in (q–p) space after the reduction in effective stress due to seismically induced pore pressure measured in P3 (see **Fig. 13**). The piezometric $r_{u,seismic}$ value is within the range of Marcuson et al. (1990) sand relationship as shown by red dot in **Fig. 6**, which reinforces the use of this shear-induced pore-water pressure relationship. Therefore, a yield strength was applied to segment 5 in the post-triggering stability analysis.

To estimate a liquefied shear strength ratio for each hydraulic sand fill segment (#1, #2, and #4), SPT penetration blow counts were converted to CPT tip resistance using the $q_c/N_{60}$ conversion proposed by Stark and Olson (1995). The approximate $D_{50}$, i.e., grain diameter at 50% passing by weight, of USFD hydraulic sand fill is assumed to be the same as Lower San Fernando Dam (LSFD), i.e., 0.12 mm, because the hydraulic fill in both dams is similar (Seed et al., 1973). Using $q_c/N_{60}$ of 0.41 and normalizing to the atmospheric pressure of 101 kPa results in a representative $q_{c1N\text{-}cs}$ value of 61.3, 68.2, 60.9 for segments #1, #2, and #4, respectively. The converted $q_{c1N\text{-}cs}$ value for segments #1, #2, and #4 show good agreement with the nearby CPT tip resistance (see CPT 5 and CPT 6 in **Fig. 11**) reported in Bardet and Davis (1996) (see **Fig. 14**). Based on the converted $q_{c1N\text{-}cs}$ values and the expression in Eqn. (20), a liquefied shear strength for segments #1, #2, and #4 were estimated to be 9, 15, and 11 kPa, respectively. A yield strength ratio for segment 5 is calculated to be 0.3 based on data in **Fig. 9**. The mobilized yield strength ratio for segment 3 is 0.22, which is typical for clay (Terzaghi et al., 1996).

With a strength ratio applied to the five segments along the estimated failure surface shown in **Fig. 11**, the resulting $FoS_{Flow}$ is 1.09, so there is potential for liquefaction-induced deformations and progressive failure of the structure. Therefore, the USFD case history indicates the proposed five-step procedure gives a reasonable explanation of the small to moderate downstream liquefaction-induced deformations occurring shortly after the earthquake on February 9, 1971.

It should be noted that there are some uncertainties related to the application of the five steps procedure for USFD case history. For example, the estimated ground motion level might be higher without direct measurement of PGA time history, the measured SPT data might avoid the weak layer which might cause slight overestimation of the $FoS_{Flow}$. The conversion of SPT data to CPT data might also introduce some uncertainties. However, the overall calculated value of $FoS_{Flow}$ = 1.09 matches the actual deformation condition.

**EXAMPLE #2 – Fundão Tailings dam failure**

This case focuses on pore-water pressure accumulation in loose sandy tailings during three (3) earthquakes within four minutes and the accompanying decrease in effective stress and FoS to assess the dynamic stability of the Fundão Tailings Dam, which failed on 5 November 2015 in **Fig. 15**. The dam experienced three ground motions within 4 minutes. The PGA of the foreshock, mainshock, and aftershock are 0.06g, 0.08g and 0.06g, respectively. A cross-section of the dam is shown in **Fig. 15**. The lowest $q_{c1}$ for soil profiles on the sand slope, plateau, and toe are 7.5, 10 and 2.5 MPa, respectively. The $FoS_{Liquefaction}$ for the sand slope are 2.08, 1.58 and 2.08 for the foreshock, mainshock, and aftershock, respectively. Similarly, the $FoS_{Liquefaction}$ for the sand plateau profile are 2.9, 2.18 and 2.9, respectively. The $FoS_{Liquefaction}$ for the sand toe profile are 1.8, 1.5 and 1.8, respectively. The corresponding pore-water pressure generation during these three earthquakes are shown in **Table 8**. With the generated excess pore-water pressures, the $Sand_{Toe}$ and $Sand_{Slope}$ stress conditions cross the critical state line as shown in **Fig. 16**. As a result, a liquefied shear strength was assigned to the $Sand_{Toe}$ and $Sand_{Slope}$ segments of the observed failure surface in the post-triggering/flow failure stability analysis. The excess pore-water pressures were included in the $Sand_{Plateau}$ profile because this segment did not mobilize liquefied strength, and a drained friction was applied to this segment (Stark et al., 2023). The observed failure surface with the strengths described above applied to the $Sand_{Slope}$, $Sand_{Plateau}$, and $Sand_{Toe}$ profiles yields a $FoS_{Flow}$ of about unity, which is in agreement with the observed failure. Additional details of this inverse analysis and case history are presented in Stark et al. (2023). This study is analyzed with few available CPT data within zone of interest. Some weak zones might not be detected during the process. The ground motion level is estimated after site failure which also introduces uncertainties into this case history.

## SUMMARY AND RECOMMENDATIONS

A five-strep procedure is proposed to assess whether a liquefied strength or liquefied strength ratio should be applied to a segment(s) along a potential failure surface in a static or dynamic stability analysis to assess the flow failure potential of dams, embankments, and slopes. This procedure consists of the following five main steps to assess the flow failure potential, which no longer include assessing contractive/dilative shear behavior: (1) assess static liquefied strength potential of segments along failure surface using **Fig. 2** or **Fig. 3**; (2) assess seismic liquefied strength potential along a potential failure surface using **Fig. 4** or **Fig. 5** for a quick estimate and then by calculating $FoS_{Liquefaction}$, i.e., ratio of cyclic resistance ratio/cyclic stress ratio, (3) if liquefaction is not triggered in any of these segments, i.e., $FoS_{Liquefaction}$ greater than unity, assess the magnitude of shear-induced pore-water pressures due to small seismic or other vibratory events of any amplitude in each segment using **Fig. 6**; (4) assign a liquefied strength to zone(s) that experience seismic liquefaction, i.e., $FoS_{Liquefaction}$ less than unity, significant pore-water pressure generation, i.e., total (static plus dynamic) pore-water pressure ratio greater than or equal to 0.7 or the updated stress path pass the critical state line using **Fig. 7** or **Fig. 8**; and (5) conduct a post-triggering stability analysis to assess flow failure potential. It should be noted that extrapolation beyond the available case history data set is not recommended in all steps.

Most flow failures can be prevented by avoiding mobilization of a liquefied strength over a significant portion of a potential failure surface. This can be evaluated using cone and/or standard penetration test results, the five-step procedure described above, and proper assessment of possible seismic, vibratory, construction, and drilling events. If a dam is estimated to be susceptible to flow failure, buttressing, draining or excavation, and/or other remedial measures should be implemented without significant vibrations or pressures to protect the structure.


**FUNDING STATEMENT**

The contents and views in this paper are those of the individual authors and do not necessarily reflect those of anyone else. The first author also appreciates the financial support of the National Science Foundation (NSF Award CMMI-1562010). The contents and views in this paper are those of the individual authors and do not necessarily reflect those of the National Science Foundation.


**COMPETING INTERESTS STATEMENT**

The authors declare that there are no competing interests.

**DATA AVAILABILITY STATEMENT**

Some or all data, models, or code generated or used during the study are available from the first author by request.

**REFERENCES**


Baziar, M.H., and Dobry, R. (1995). ‘‘Residual strength and large- deformation potential of loose silty sands.’’ *J. Geotech. Eng.*, **121**(12), 896–906.

Beaty, M.H. and Byme, P.M., (2001). “Observations on the San Fernando dams.” *Proc., 4th Int. Conf. on Recent Advances in Geotechnical Earthquake Engineering and Soil Dynamics*, Univ. of Missouri-Rolla, Rolla, MO, 339–347.

Beaty, M., Byrne, P., 2011. UBCSAND constitutive model, Version 904aR. Documentation Report: UBCSAND constitutive model on Itasca UDM Web Site.

Been, K., Conlin, B.H., Crooks, J.H.A., Fitzpatrick, S.W., Jefferies, M.G., Rogers, B.T., and Shinde, S. (1987). ‘‘Back analysis of the Nerlerk berm liquefaction slides: Discussion.’’ *Can. Geotech. J.*, **24**, 170– 179.

Boulanger, R. and Idriss, I. (2014). *CPT and SPT Based Liquefaction Triggering Procedures, Rep. No. UCD/CGM-14/01*, University of California at Davis, Department of Civil and Environmental Engineering, 2014, at 1–23.

Boulanger, R. W. and Ziotopoulou, K. PM4Silt (Version 1): A Silt Plasticity Model for Earthquake Engineering Applications. Davis, CA: Center for Geotechnical Modeling, Department of Civil and Environmental Engineering, University of California, USA; 2018. Report No. UCD/CGM18/01

Castro, G., Keller, T.O., and Boynton, S.S. (1989). ‘‘Re-evaluation of the Lower San Fernando Dam: Report 1, an investigation of the February 9, 1971 slide.’’ *U.S. Army Corps of Engineers Contract Rep. No. GL-89-2*, Vols. 1 and 2, U.S. Army Corps of Engineers Waterways Experiment Station, Vicksburg, Miss.

Chowdhury, K., Seed, R.B., Dreger, D.S., Perlea, V., Beaty, M., Ma, F., & Wang, Z.L. (2018). “Re-Evaluation of the Performance of the Upper San Fernando Dam: A Liquefaction-Induced Moderate Deformation Case History.” *Geotechnical Earthquake Engineering and Soil Dynamics V: Liquefaction Triggering, Consequences, and Mitigation* (pp. 518-534). Reston, VA: American Society of Civil Engineers.

Eckersley, D. (1990). ‘‘Instrumented laboratory flow slides.’’ *Geotechnique,* **40**, 489–502.

Fear, C.E., and Robertson, P.K. (1995). ‘‘Estimating the undrained strength of sand: A theoretical framework.’’ *Can. Geotech. J.,* **32**(4), 859– 870.

Hanzawa, H. (1980). ‘‘Undrained strength and stability analysis for a quick sand.’’ *Soils Found.,* **20**(2), 17–29.

Hanzawa, H., Itoh, Y., and Suzuki, K. (1979). ‘‘Shear characteristics of a quick sand in the Arabian Gulf.’’ *Soils Found.,* 19(4), 1–15.

Harder, L.F., Jr., and Boulanger, R. (1997). ‘‘Application of $K_{\sigma}$ and $K_{\alpha}$ correction factors.’’ *Proc., NCEER Workshop on Evaluation of Liquefaction Resistance of Soils*, T. L. Youd and I. M. Idriss, eds., NCEER- 97-0022, 167–190.

Hedien, J.E., Anderson, R.J., and Niznik, J.A. (1998). ‘‘Evaluation of liquefaction potential and seismic safety for Tennessee Valley Authority embankment dams.’’ *Proc., Conf. on Current Earthquake Engineering Research in the Central United States* (CEERICUS’98), D. F. Laefer and J. P. Arnett, eds., Univ. of Illinois-Urbana-Champaign, April 4, II-1–II-8.

Hidayat, R.F., Kiyota,T., Tada, N., Hayakawa, J., and Nawir, H. (2020). “Reconnaissance on liquefaction-induced flow failure caused by the 2018 Mw 7.5 sulawesi earthquake, palu, Indonesia,” *J. Eng. Technol. Sci.,* **52**(1), 51–65.

Mason, H.B., Montgomery, J., Gallant, A.P., et al. (2021). “East Palu Valley flowslides induced by the 2018 MW 7.5 Palu-Donggala earthquake”, Geomorphology, 373, 107482, 17p, https://doi.org/10.1016/j.geomorph.2020.107482.

Hicks, M.A., and Boughrarou, R. (1998). ‘‘Finite element analysis of the Nerlerk underwater berm failures.’’ *Geotechnique,* **48**(2), 169–185.

Idriss, I.M. and Boulanger, R.W. (2008). Soil Liquefaction during Earthquakes.” Engineering Monographs on Earthquake Criteria, Structural Design, and Strong Motion Records. Monograph #12, MON-12, Earthquake Engineering Research Institute, EERI, 499 14th Street, Suite 320, Oakland, CA 94612, http://www.eeri.org, 237.

Idriss, I.M. and Boulanger, R.W. (2015). “2nd Ishihara Lecture: SPT- and CPT-based relationships for the residual shear strength of liquefied soils.” *Soil Dynamics and Earthquake Engineering,*Volume 68, Pages 57-68, https://doi.org/10.1016/j.soildyn.2014.09.010.

Ishihara, K. (1984). ‘‘Post-earthquake failure of a tailings dam due to liquefaction of the pond deposit.’’ *Proc., Int. Conf. on Case Histories in Geotechnical Engineering*, Rolla, Mo., May 6–11, 3, 1129–1143.

Ishihara, K. (1993). ‘‘Liquefaction and flow failure during earthquakes.’’ *Geotechnique,* **43**(3), 351– 415.

Kayen, R.E., Mitchell, J.K., Seed, R.B., Lodge, A., Nishio, S., and Coutinho, R. (1992). “Evaluation of SPT-, CPT-, and shear wave based methods for liquefaction potential assessments using Loma Prieta data. *Proc., 4th Japan–U.S. Workshop on Earthquake Resistant Design of Lifeline Facilities and Countermeasures for Soil Liquefaction*, Honolulu, Hawaii. Vol. 1, pp. 177–192.

Kramer, S.L. and Wang, C-H. 2015. Empirical model for estimation of the residual strength of liquefied soil. *J. Geotechnical and Geoenvironmental Eng.*, ASCE, **141**(9): 1-15.

Kuerbis, R., Negussey, D., and Vaid, Y.P. (1988). ‘‘Effect of gradation and fines content on the undrained response of sand.’’ *Hydraulic fill structures*, ASCE Geotechnical Engineering Division Specialty Publication No. 21, D. J. A. Van Zyl and S. G. Vick, eds., Fort Collins, Colo., 330–345.

Muhammad, K. (2012). “Case history – based analysis of liquefaction in slope ground.” PHD. Dissertation. University of Illinois at Urbana Champaign.

Makdisi, F.I., and Seed, H.B. (1978). ‘‘Simplified procedure for estimating dam and embankment earthquake-induced deformations.’’ *J. Geo- tech. Eng. Div., Am. Soc. Civ. Eng.,* **104**(7), 849– 867.

Mesri, G. (2007). ‘‘Yield strength and critical strength of liquefiable sands in sloping ground.’’ *Geotechnique,* **57**(3), 309-311.

Miura, K., Yoshida, N., Nishimura, M., and Wakamatsu, K. (1998). ‘‘Stability analysis of the fill embankment damaged by recent two major earthquakes in Hokkaido, Japan.’’ *Proc., 1998 Geotechnical Earth- quake Engineering and Soil Dynamics Specialty Conf.,* ASCE Geo-Institute Geotechnical Specialty Publication No. 75, Vol. 2, August 3– 6, Seattle, 926–937.

Morgenstern, N.R., Vick, S.G., Viotti, C.B., and Watts, B.D. (2016). “Fundão Tailings Dam Review Panel: Report on the immediate causes of the failure of the Fundão Dam.” Report prepared for Cleary Gottlieb Steen & Hamilton LLP, New York, http://fundaoinvestigation.com/the-panel-report/.

Olson, S.M. (2001). ‘‘Liquefaction analysis of level and sloping ground using field case histories and penetration resistance.’’ PhD thesis, Univ. of Illinois-Urbana-Champaign, Urbana, Ill. 549 p. (available at http://pgi-tp.ce.uiuc.edu/olsonwebfiles/olsonweb/index.htm)

Olson, S.M., Stark, T.D., Walton, W.H., and Castro, G. (2000). ‘‘1907 Static liquefaction flow failure of North Dike of Wachusett Dam.’’ *J. Geotech. Geoenviron. Eng.,* **126**(12), 1184 – 1193.

Olson, S.M., and Stark, T.D. (2001). ‘‘Liquefaction analysis of Lower San Fernando Dam using strength ratios.’’ *Proc., Fourth Int. Conf. on Recent Advances in Geotechnical Earthquake*

*Engineering and Soil Dynamics*, S. Prakash, ed., San Diego. Paper 4.05.

Olson, S.M., and Stark, T.D. (2002). ‘‘Liquefied strength ratio from liquefaction flow failure case histories.’’ *Can. Geotech. J.*, **39**(3), 629– 647.

Olson, S.M., and Stark, T.D. (2003). ‘‘Yield strength ratio and liquefaction analysis of slopes and embankments.’’ *J. Geotech. Eng.*, **129**(8), 727– 737.

Ovando-Shelley, E., and Perez, B.E. (1997). ‘‘Undrained behavior of clayey sands in load controlled triaxial tests.’’ *Geotechnique*, **47**(1), 97–111.

Pillai, V.S., and Stewart, R.A. (1994). ‘‘Evaluation of liquefaction potential of foundation soils at Duncan Dam.’’ *Can. Geotech. J.*, **31**, 951–966.

Pitman, T.D., Robertson, P.K., and Sego, D.C. (1994). ‘‘Influence of fines on the collapse of loose sands.’’ *Can. Geotech. J.*, **31**, 728 –739.

Poulos, S.J. (1988). ‘‘Liquefaction and related phenomena.’’ *Advanced dam engineering for design, construction, and rehabilitation*, R. B. Jansen, ed., Van Nostrand Reinhold, New York, 292–320.

Poulos, S.J., Castro, G., and France, W. (1985a). ‘‘Liquefaction evaluation procedure.’’ *J. Geotech. Eng.*, **111**(6), 772–792.

Poulos, S.J., Robinsky, E.I., and Keller, T.O. (1985b). ‘‘Liquefaction resistance of thickened tailings.’’ *J. Geotech. Eng.*, **111**(12), 1380– 1394.

Robertson, P.K., Melo, L., Williams, D. and Wilson, G.W. (2019) *Report of the Expert Panel on the Technical Causes of the Failure of Feijão Dam I*, http://www.b1technicalinvestigation.com/.

Robertson, P.K., (2010) “Evaluation of Flow Liquefaction and Liquefied Strength Using the Cone Penetration Test” Journal of Geotechnical And Geoenvironmental Engineering, ASCE.

136 (6) 842- 853.

Robertson, P.K., (2021) “Evaluation of flow liquefaction and liquefied strength using the cone penetration test: an update” *Can. Geotech. J*. 00: 1–5 (0000) dx.doi.org/10.1139/cgj-2020-0657

Rogers, B.T., Been, K., Hardy, M.D., Johnson, G.J., and Hachey, J.E. (1990). ‘‘Re-analysis of Nerlerk B-67 berm failures.’’ *Proc., 43rd Can. Geot. Conf.—Prediction of Performance in Geotechnique,* Quebec, Canada, **1**, 227–237.

Sasitharan, S., Robertson, P.K., Sego, D.C., and Morgenstern, N.R. (1993). ‘‘Collapse behavior of sand.’’ *Can. Geotech. J.,* **30**, 569–577.

Seed, R B., and Harder, L.F. (1990). ‘‘SPT-based analysis of cyclic pore pressure generation and undrained residual strength.’’ *Proc., H.B.Seed Memorial Symp.*, Bi-Tech Publishing Ltd., 2, 351–376.

Seed, H.B., and Idriss, I.M. (1971). ‘‘Simplified procedure for evaluating soil liquefaction potential.’’ *J. Soil Mech. Found. Div., Am. Soc. Civ. Eng.,* **97**(9), 1249–1273.

Seed, H.B., Lee, K.L., Idriss, I.M., and Makdisi, F. (1973). “Analysis of the slides in the San Fernando Dams during the earthquake of February 9, 1971.” Report No. EERC 73-2, Earthquake Engineering Research Center, University of California, Berkeley.

Seed, H.B., Seed, R.B., Harder, L.F., and Jong, H.-L. (1989). ‘‘Re-evaluation of the Lower San Fernando Dam: Report 2, examination of the post-earthquake slide of February 9, 1971.’’ *U.S. Army Corps of Engineers Contract Rep. No. GL-89-2*, U.S. Army Corps of Engineers Waterways Experiment Station, Vicksburg, Miss.

Seed, H.B., Tokimatsu, K., Harder, L.F., and Chung, R. (1985). ‘‘The influence of SPT procedures in soil liquefaction resistance evaluations.’’ *J. Geotech. Eng.,* **111**(12), 1425–

1445.

Serff, N., Seed, H. B., Makdisi, F. I., and Chang, C. -Y.(1976). “Earthquake-induced deformations of earth dams”,Report EERC 76-4, Earthquake Engineering Research Center, University of California, Berkeley, CA.

Skempton, A.W. (1986). “Standard penetration test procedures and the effects in sands of overburden pressure, relative density, particle size, aging and overconsolidation.” *Geotechnique,* **36**(3), 425-447.

Sladen, J.A., D’Hollander, R.D., and Krahn, J. (1985). ‘‘The liquefaction of sands, a collapse surface approach.’’ *Can. Geotech. J.,* **22**, 564 – 578.

Sladen, J.A., D’Hollander, R.D., Krahn, J., and Mitchell, D.E. (1987). ‘‘Back analysis of the Nerlerk berm liquefaction slides: Reply.’’ *Can. Geotech. J.*, **24**, 179–185.

Sladen, J.A., and Hewitt, K.J. (1989). ‘‘Influence of placement method on the in situ density of hydraulic sand fills.’’ *Can. Geotech. J.,* **26**, 453– 466.

Spencer, E. (1967). ‘‘A method of analysis of the stability of embankments assuming parallel inter-slice forces.’’ *Geotechnique,* **17**(1), 11– 26.

Stark, T.D. and Contreras, I.A. (1998). "Fourth Avenue Landslide During 1964 Alaskan Earthquake." *J. Geotech. Geoenv. Engrg. Div.*, ASCE, **124**(2), 99-109.

Stark, T.D., Lin, J., and Gimmes, E. (2023). ‘‘Pore-Water Pressure Accumulation During Closely Spaced Earthquakes: Fundão Tailings Dam.’’ *J. Applied Earth Science*, accepted for publication.

Stark, T.D. and Olson, S.M. (1995). ‘‘Liquefaction resistance using CPT and field case histories.’’ *J. Geotech. Eng.,* **121**(12), 856 – 869.

Stark, T.D., Beaty, M.H., Castro, G., Walberg, F.C., Nicholson, P.J., Perlea, V.G., Axtell, P.J., Dillon, J.C., Empson, W.B., and Mathews, D.L. (2012). "Seismic Deformation Analysis of Tuttle Creek Dam," *Canadian Geotech. Journal*, **49**, 323-343.

Terzaghi, K., Peck, R.B., and Mesri, G. (1996). *Soil mechanics in engineering practice*, 3rd Ed., Wiley, New York.

Tokimatsu, K. and Seed, H.B. (1987). "Evaluation of settlements in sands due to earthquake shaking." *Journal of Geotechnical Engineering*, ASCE, **113**(8): 861–878.

Vaid, Y.P., and Chern, J.C. (1985). ''Cyclic and monotonic undrained response of saturated sands.'' *Proc., Advances in the Art of Testing Soils under Cyclic Conditions*, V. Khosla, ed., ASCE, New York, 120–147.

Weber, J.P. (2015). "Engineering evaluation of post-liquefaction strength." PhD thesis, Univ. of California, Berkeley.

Wright, S.G. (1992). *UTEXAS3: A computer program for slope stability calculations*, Geotechnical Engineering Software GS86-1, Dept. of Civil Engineering, Univ. of Texas, Austin.

Yamamuro, J.A., Covert, K.M., and Lade, P.V. (1999). ''Static and cyclic liquefaction of silty sands.'' *Proc., Int. Workshop on the Physics and Mechanics of Soil Liquefaction*, P. V. Lade and J. A. Yamamuro, eds., Baltimore, 55– 65.

Yegian, M.K., Ghahraman, V.G., and Harutinunyan, R.N. (1994). ''Liquefaction and embankment failure case histories, 1988 Armenian earthquake.'' *J. Geotech. Eng.*, **120**(3), 581–596.

Youd, T.L., and Idriss, I.M., Eds. (1997). ''Summary report.'' *Proc., NCEER Workshop on Evaluation of Liquefaction Resistance of Soils*, NCEER-97-0022, 1– 40.

## TABLES & CAPTIONS

**Table 1. Static flow failure case histories used in Fig.2**

| Structure | Cause of Failure | Vertical effective stress (kPa) | $q_{c1}$ (MPa) | | | Sources |
|---|---|---|---|---|---|---|
| | | | BE | LB | UB | |
| Cadia | 2018 progressive softening | 166 | 0.8 | 0.2 | 1.6 | Morgenstern et al. (2019) |
| Feijão Tailings Dam | 2019 unknown | 174.8 | 1.4 | 0.9 | 1.8 | Robertson et al. (2019) |
| Zeeland — Vlietepolder | 1889 High tide | 59.7 | 3 | 1.7 | 4.4 | Olson and Stark (2003) |
| Wachusett Dam — north dike | 1907 Reservoir filling | 141.6 | 4.6 | 2.6 | 6.5 | |
| Calaveras Dam | 1918 Construction | 294.3 | 5.5 | 1 | 6 | |
| Helsinki Harbor | 1936 Construction | 15.1 | 4 | - | - | |
| Fort Peck Dam | 1938 construction | 319.7 | 3.4 | 1.6 | 5.6 | |
| Tar Island Dyke | 1974 Construction | 135.8 | 3 | 2 | 4 | |
| Sullivan Tailings Dam | 1991 Construction | 110 | 1.38 | 0.97 | 2.26 | Muhamad (2012) |
| Merrispurit Dam | 1994 Strong Rainfall | 240 | 0.64 | - | - | |
| Jamuna Bridge 1500W3 | 1995 Dredging at the slope toe | 59 | 2.9 | 1.9 | 4 | |

**Table 2. Static flow failure case histories used in Fig. 3**

| Reference | Name | qc1 (Mpa) | Vertical Effective Stress (kPa) | Fine content (%) | m | $q_{c1N}$ | Δqc1N | $q_{c1N\text{-}cs}$ | liquefied strength (kPa) |
|---|---|---|---|---|---|---|---|---|---|
| Morgenstern et al. (2019) | Cadia tailings dam | 0.8 | 166.00 | 60 | 0.94 | 7.92 | 50.38 | 58.30 | 13.28 |
| Robertson et al. (2019) | Feijão dam | 1.40 | 174.80 | 55 | 0.84 | 13.86 | 51.28 | 65.14 | 13.98 |
| Olson and Stark (2002) | Zeeland - Vlietepolder | 3.00 | 59.70 | 11 | 0.73 | 29.70 | 7.81 | 36.76 | 7.47 |
| | Wachusett Dam - North Dike | 4.60 | 141.60 | 8 | 0.66 | 45.54 | 2.46 | 47.00 | 14.08 |
| | Calaveras Dam | 5.50 | 294.30 | 34 | 0.60 | 54.46 | 51.76 | 112.46 | 35.87 |
| | Helsinki Harbor | 4.00 | 15.10 | 0 | 0.65 | 39.60 | 0.00 | 47.73 | 2.30 |
| | Fort Peck Dam | 3.40 | 319.7 | 54 | 0.71 | 32.67 | 56.16 | 89.08 | 36.49 |
| | Tar Island Dyke | 3.00 | 135.80 | 13 | 0.74 | 29.70 | 12.33 | 40.00 | 24.71 |
| Muhammad (2012) | Sullivan Tailings | 1.38 | 110.00 | 88 | 0.85 | 13.66 | 56.93 | 70.18 | 13.27 |
| | Merrispurit Dam | 0.64 | 240 | 30 | 0.93 | 6.34 | 36.54 | 42.88 | 12.00 |
| | Jamuna Bridge | 2.90 | 59 | 17 | 0.73 | 28.71 | 21.54 | 51.06 | 8.38 |

**Table 3. Seismic/Dynamic induced flow failure case histories from Olson and Stark (2003)**

| Case History/Location | Cause of Failure | Loading Condition | Year of failure | Case History | Weighted average prefailure vertical effective stress (kPa) | Weighted average prefailure vertical total stress' (kPa) | $q_{c1}$ (MPa) | | |
|---|---|---|---|---|---|---|---|---|---|
| | | | | | | | BE | LB | UB |
| Sheffield Dam | 1925 Santa Barbara eq. ($M_L$ = 6.3) | Seismic | 1925 | 4 | 68.4 | 84.3 | 2.20 | 1.80 | 2.60 |
| Solfatara Canal Dike | 1940 Imperial Valley eq. ($M_L$= 7.1) | Seismic | 1940 | 7 | 26.5 | 37.8 | 2.50 | - | - |
| Lake Merced bank | 1957 San Francisco eq. ($M_L$= 5.3) | Seismic | 1957 | 8 | 55.4 | 89.1 | 3.20 | 3.00 | 6.20 |
| Kawagishi-Cho building | 1964 Niigata eq. ($M_W$= 7.5) | Seismic | 1964 | 9 | | | 3.10 | 3.00 | 3.80 |
| Uetsu Railway embankment | 1964 Niigata eq. ($M_W$= 7.5) | Seismic | 1964 | 10 | 51.7 | 59.4 | 1.80 | - | - |
| El Cobre Tailings Dam | 1965 Chilean eq. ($M_L$= 7 to 7.25) | Seismic | 1965 | 11 | | | 0.00 | - | - |
| Koda Numa Highway embankment | 1968 Tokachi-Oki eq. ($M_L$= 7.9) | Seismic | 1968 | 12 | 20.9 | 23.9 | 1.35 | - | - |
| Metoki Road embankment | 1968 Tokachi-Oki eq. ($M_L$= 7.9) | Seismic | 1968 | 13 | 34.8 | 42.9 | 1.05 | 0.90 | 1.20 |
| Hokkaido Tailings Dam | 1968 Tokachi-Oki eq. ($M_L$= 7.9) | Seismic | 1968 | 14 | 59.9 | 70.2 | 0.36 | 0.35 | 0.38 |
| Lower San Fernando Dam | 1971 San Fernando eq. ($M_W$= 6.6) | Seismic | 1971 | 15 | | | 4.70 | 2.10 | 6.20 |
| Mochi-Koshi Tailings Dam — Dike 1 | 1978 Izu-Oshima-Kinkai eq. ($M_L$= 7.0) | Seismic | 1978 | 17 | 73.8 | 116.1 | 0.50 | 0.25 | 1.00 |
| — Dike 2 | | Seismic | 1978 | 18 | 69.2 | 110.0 | 0.50 | 0.25 | 1.00 |
| Hachiro-Gata Road embankment | 1983 Nihon-Kai-Chubu eq. ($M$ = 7.7) | Seismic | 1983 | 22 | 30.2 | 36.9 | 3.00 | 1.10 | 4.90 |
| Asele road embankment | 1983 Pavement repairs | Dynamic | 1983 | 23 | 59.9 | | 4.00 | 3.40 | 4.60 |
| La Marquesa Dam —U/S slope | 1985 Chilean eq. ($M_s$ = 7.8) | Seismic | 1985 | 24 | 46.0 | 101.0 | 2.00 | 1.80 | 2.30 |

| | | | | | | | | | |
|---|---|---|---|---|---|---|---|---|---|
| —D/S slope | | Seismic | 1985 | 25 | 51.4 | 58.4 | 4.10 | 3.20 | 5.00 |
| La Palma Dam | 1985 Chilean eq. ($M$s = 7.8) | Seismic | 1985 | 26 | 39.7 | 57.6 | 1.80 | 1.00 | 2.50 |
| Fraser River Delta | 1985 Gas desaturation and low tide | Seismic | 1985 | 27 | | | 2.90 | 1.30 | 4.50 |
| Chonan Middle School | 1987 Chiba-Toho-Oki eq. ($M$ = 6.7) | Seismic | 1987 | 29 | 56.4 | 64.8 | 2.60 | 1.80 | 4.40 |
| Nalband railway embankment | 1988 Armenian eq. (Ms, = 6.8) | Seismic | 1988 | 30 | 48.9 | 78.8 | 6.00 | 2.30 | 8.10 |
| Soviet Tajik —May 1 slide | 1989 Tajik, Soviet Union eq. ($M_L$ = 5.5) | Seismic | 1989 | 31 | 106.0 | 170.4 | 1.90 | 1.10 | 2.40 |
| Shibecha-Cho embankment | 1993 Kushiro-Oki eq. ($M$ = 7.8) | Seismic | 1993 | 32 | 66.6 | 81.7 | 2.80 | 1.50 | 5.40 |
| Route 272 at Higashiarekinai | 1993 Kushiro-Oki eq. ($M$ = 7.8) | Seismic | 1993 | 33 | 52.3 | 71.1 | 3.20 | 1.20 | 5.00 |

**Table 4. Seismic induced flow failure case histories from Muhamad (2012).**

| | | | | | $q_{c1}$ (MPa) | | | σ′v |
|---|---|---|---|---|---|---|---|---|
| Case No. | Year | Structure Name | Penetration Data | FC (%) | BE | U/B | L/B | Effective Vertical Stress (kPa) |
| 1 | 1928 | Barahona Dam | SPT;CPT | 15-20 | 3.5 | 11 | 0.6 | 404 |
| 2 | 1979 | Kamenari Landslide | SPT | - | 3.8 | 6.9 | 0.8 | 51 |
| 3 | 1988 | Spitak Embankment slide 1 | SPT;CPT | 0 | 7.8 | 9.2 | 4.6 | 46.5 |
| 4 | 1988 | Spitak Embankment slide 2 | SPT;CPT | 0 | 7.8 | 9.2 | 4.6 | 47 |
| 5 | 1989 | Okuli Landslide | SPT | 100 | 0.8 | 1.9 | 0.66 | 113 |
| 6 | 1991 | Sullivan Tailings Dam | SPT;CPT | 88 | 1.38 | 2.26 | 0.97 | 110 |
| 7 | 1993 | Kushiro River Right Bank | SPT | 10 | 1.7 | 2.3 | 0 | 56 |
| 8 | 1993 | Kushiro River Left Bank | SPT | 10 | 1.7 | 4 | 1.14 | 79 |
| 9 | 1993 | Tohnai Dike | SPT | 10 | 2.4 | 5.2 | 2 | 89 |
| 10 | 1993 | Pashikuru (Route 38) Road Embankment | SPT | 20 | 1.68 | - | - | 93.5 |
| 11 | 1993 | Itoizawa (Route 44) Road Embankment | SPT | 20 | 2.8 | 5.6 | 2.24 | 56 |
| 12 | 1994 | Merrispurit Dam | CPT | 1-60 | 0.64 | - | - | 240 |
| 13 | 1994 | King Harbor Mole B | SPT;CPT | 2-7 | 4.6 | 11.7 | 1.1 | 47 |
| 14 | 1995 | Torishima Dike | SPT | 20 | 2.7 | 5 | 0.9 | 58.5 |
| 15 | 1995 | Nishijima Dike | SPT | 20 | 3.68 | 6.44 | 1.38 | 44 |
| 16 | 1995 | Upper Niteko Dam | SPT | 15 | 3.1 | 6.7 | 2.6 | 42 |
| 17 | 1995 | Middle Niteko Dam | SPT | 15 | 2.55 | 3.06 | 1.53 | 65 |
| 18 | 1995 | Takarazuka Landslide | SPT | 0 | 7.15 | 11.7 | 2.6 | 104 |
| 19 | 1995 | Nikawa Landslide | SPT | 17 | 4.95 | 7.7 | 2.2 | 175 |
| 20 | 1995 | Idenoshiri Dam | SPT | 30 | 2.4 | 4 | 1.6 | 87.5 |
| 21 | 1995 | Jamuna Bridge 1500W3 | SPT;CPT | 15-20 | 2.9 | 3.6 | 2.5 | 60 |
| 22 | 1996 | Jamuna Bridge 1800W4 | SPT;CPT | 15-20 | 3 | 3.9 | 2.5 | 54.5 |
| 23 | 1996 | Jamuna Bridge 1800WT13 | SPT;CPT | 15-20 | 3 | 3.5 | 2.4 | 69 |
| 24 | 1996 | Jamuna Bridge 2500WT4 | SPT;CPT | 15-20 | 2.8 | 4 | 1.9 | 53.5 |
| 25 | 1999 | Degimendere Slope | SPT;CPT | 5-10 | 2.8 | 4 | 1.9 | 53.5 |
| 26 | 2001 | Chang Dam | SWS | 15-23 | 4.8 | 6.24 | 3.84 | 105 |
| 27 | 2001 | Shivlakha Dam | Estimated | 15-23 | 4.8 | 5.8 | 3.84 | 112.5 |
| 28 | 2001 | Tapar Dam | Estimated | 15-23 | 4.8 | 5.8 | 3.84 | 102.25 |
| 29 | 2001 | Fategadh Dam | SPT | 15-23 | 5.76 | 7.2 | 4.8 | 83 |
| 30 | 2001 | Kaswati Dam | SPT | 15-23 | 5.76 | 7.2 | 4.3 | 88.5 |
| 31 | 2001 | Suvi Dam | Estimated | 15-23 | 4.8 | 5.8 | 3.84 | 104.5 |

**Table 5. Flow failure case histories analyzed herein.**

| Structure | Cause of Failure | Acceleration (g) | Depth (m) | CSR | CRR | Vertical total stress (kPa) | Vertical effective stress (kPa) | $q_{c1}$ (MPa) | | | | FoS |
|---|---|---|---|---|---|---|---|---|---|---|---|---|
| | | | | | | | | BE | UB | LB | | |
| Las Palas Tailings Dam | 2010 Chile eq. ($M_W$= 8.8) | 0.48 | 13.10 | 0.31 | 0.10 | 196.50 | 196.50 | 1.75 | 2.10 | 0.70 | | 0.23 |
| Yamanaka Dam | 1968 Tokachi-Oki eq. ($M_W$= 8.3) | 0.06 | 0.60 | 0.22 | 0.13 | 30.10 | 5.10 | 4.70 | - | - | | 0.62 |
| Kayakari Dam | 2011 Tōhoku eq. ($M_W$= 9.0) | 0.42 | 5.50 | 0.32 | 0.06 | 101.83 | 86.79 | 1.24 | 2.16 | 1.05 | | 0.18 |
| Fundão Slope | 2015 near source eq. ($M_L$ = 2.6) | 0.08 | 4.60 | 0.06 | 0.10 | 100.65 | 91.49 | 7.30 | 10.22 | 7.30 | | 1.58 |
| Fundão Toe | 2015 near source eq. ($M_L$ = 2.6) | 0.08 | 4.30 | 0.06 | 0.08 | 94.38 | 91.54 | 2.70 | 8.80 | 2.70 | | 1.49 |
| Fundão Plateau (not liquefied) | 2015 near source eq. ($M_L$ = 2.6) | 0.08 | 5.00 | 0.04 | 0.09 | 110.00 | 110.00 | 10.0 | 12.81 | 7.92 | | 2.10 |
| Palu City | 2018 Sulawesi eq. ($M_W$= 7.5) | 0.29 | 4.00 | 0.44 | 0.07 | 68.00 | 28.00 | 1.08 | 5.39 | 0.72 | | 0.16 |
| Cadia Tailings Dam | 2018 progressive softening | Static | 7.6-15.0 | | | | 166.00 | 0.39 | - | - | | |
| Feijão Tailings Dam | 2019 unknown | Static | 6.0-19.0 | | | | 174.80 | 1.40 | 1.80 | 0.90 | | |

**Table 6.** **Flow failure case histories analyzed herein with fine content correction.**

| | Case number | Name | qc1 | Vertical Effective Stress (kPa) | Fine content (%) | m | qc1N | Δqc1N | qc1Ncs | liquefied strength (kPa) | acceration (g) |
|---|---|---|---|---|---|---|---|---|---|---|---|
| Olson and Stark (2002) | 1 | Zeeland - Vlietepolder | 3.0 | 59.7 | 11.0 | 0.7 | 29.7 | 7.8 | 37.5 | 7.5 | |
| | 2 | Wachusett Dam - North Dike | 4.6 | 141.6 | 8.0 | 0.7 | 44.5 | 2.5 | 47.0 | 14.1 | |
| | 3 | Calaveras Dam | 5.5 | 294.3 | 34.0 | 0.6 | 60.7 | 51.8 | 112.5 | 35.9 | |
| | 4 | Sheffield Dam | 2.5 | 62.6 | 40.0 | 0.8 | 24.7 | 47.9 | 72.6 | 6.6 | 0.2 |
| | 5 | Helsinki Harbor | 4.0 | 15.1 | 0.0 | 0.6 | 39.6 | 0.0 | 39.6 | 2.3 | |
| | 6 | Fort Peck Dam | 3.4 | 319.7 | 54.0 | 0.7 | 32.9 | 56.2 | 89.1 | 36.5 | |
| | 7 | Solfatara Canal Dike | 3.5 | 32.0 | 0.0 | 0.7 | 34.5 | 0.0 | 34.5 | 3.1 | 0.3 |
| | 8 | Lake Merced bank | 4.0 | 39.9 | 0.0 | 0.7 | 39.6 | 0.0 | 39.6 | 6.5 | 0.1 |
| | 9 | Kawagishi-Cho building | 3.3 | 70.6 | 2.0 | 0.7 | 33.0 | 0.0 | 33.0 | 5.3 | 0.2 |
| | 10 | Uetsu Railway embankment | 2.0 | 69.3 | 0.0 | 0.8 | 19.8 | 0.0 | 19.8 | 1.8 | 0.2 |
| | 11 | El Cobre Tailings Dam | 0.1 | 99.4 | 95.0 | 1.1 | 1.0 | 53.8 | 54.8 | 4.5 | 0.8 |
| | 12 | Koda Numa highway embankment | 1.8 | 41.7 | 40.0 | 0.8 | 18.3 | 46.3 | 64.6 | 4.4 | |
| | 13 | Metoki Road embankment | 1.3 | 57.6 | 0.0 | 0.9 | 12.8 | 0.0 | 12.8 | 6.3 | |

| | | | | | | | | | | | |
|---|---|---|---|---|---|---|---|---|---|---|---|
| | 14 | Hokkaido Tailings Dam | 0.4 | 65.9 | 50.0 | 1.0 | 4.4 | 47.2 | 51.5 | 4.8 | |
| | 15 | Lower San Fernando Dam | 4.6 | 152.0 | 25.0 | 0.7 | 45.6 | 38.2 | 83.8 | 25.8 | 0.5 |
| | 16 | Tar Island Dyke | 3.0 | 201.0 | 13.0 | 0.7 | 29.7 | 12.3 | 42.0 | 24.7 | |
| | 17 | Mochi- kochi Dike 1 | 0.6 | 73.4 | 73.0 | 0.9 | 5.7 | 52.7 | 58.4 | 10.1 | 0.3 |
| | 19 | Nerlerk Berm Slide 1 | 5.8 | 29.5 | 10.0 | 0.6 | 57.4 | 6.5 | 63.9 | 3.3 | |
| | 22 | Hachiro-Gata Road embankment | 4.0 | 32.2 | 15.0 | 0.7 | 40.1 | 18.0 | 58.1 | 3.3 | 0.2 |
| | 24 | U/S slope | 2.5 | 47.0 | 20.0 | 0.8 | 24.8 | 26.8 | 51.7 | 4.9 | 0.6 |
| | 25 | DIS slope | 4.5 | 58.2 | 30.0 | 0.7 | 44.6 | 44.3 | 89.0 | 10.2 | 0.6 |
| | 26 | La Palma Dam | 2.5 | 36.7 | 15.0 | 0.8 | 24.8 | 16.7 | 41.5 | 6.5 | 0.5 |
| | 28 | Lake Ackerman highway embankment | 3.6 | 43.5 | 0.0 | 0.7 | 35.4 | 0.0 | 35.4 | 5.1 | |
| | 29 | Chonan Middle School | 2.4 | 49.4 | 18.0 | 0.8 | 23.3 | 22.9 | 46.2 | 6.8 | 0.1 |
| | 30 | Nalband Railway embankment | 6.4 | 57.9 | 30.0 | 0.6 | 63.1 | 48.1 | 111.1 | 8.0 | 0.8 |
| | 31 | Soviet Tajik - May 1 slide | 1.9 | 91.3 | 16.0 | 0.8 | 19.3 | 18.4 | 37.7 | 16.3 | 0.2 |
| | 32 | Shibecha-Cho embankment | 3.1 | 67.8 | 20.0 | 0.7 | 30.3 | 27.6 | 57.8 | 10.7 | 0.3 |
| | 33 | Route 272 at Higashiarekinai | 3.4 | 61.5 | 33.0 | 0.7 | 34.1 | 45.0 | 79.1 | 6.6 | 0.4 |
| Muhammad (2012) | 2 | Kamenari Landslide | 4.2 | 61.3 | 0.0 | 0.7 | 41.2 | 0.0 | 41.2 | 7.5 | 0.2 |

| | | | | | | | | | | | |
|---|---|---|---|---|---|---|---|---|---|---|---|
| | 3 | Spitak Embankment slide 1 | 8.2 | 51.0 | 0.0 | 0.5 | 81.2 | 0.0 | 81.2 | 7.8 | 0.8 |
| | 5 | Okuli Landslide | 4.1 | 46.5 | 100.0 | 0.7 | 40.9 | 66.6 | 107.6 | 7.0 | 0.2 |
| | 6 | Sullivan Tailings | 1.3 | 110.0 | 88.0 | 0.8 | 13.2 | 56.9 | 70.2 | 0.3 | |
| | 7 | Kushiro River Left Bank | 1.6 | 115.6 | 10.0 | 0.8 | 16.3 | 5.3 | 21.6 | 7.3 | 0.4 |
| | 9 | Tohnai Dike | 2.5 | 79.0 | 10.0 | 0.8 | 25.1 | 5.6 | 30.7 | 9.7 | 0.2 |
| | 11 | Itoizawa (Route 44) Road Embankment | 2.9 | 89.0 | 20.0 | 0.7 | 28.4 | 27.3 | 55.7 | 11.0 | 0.2 |
| | 14 | Torishima Dike | 3.1 | 56.0 | 20.0 | 0.7 | 30.8 | 27.6 | 58.5 | 13.3 | 0.3 |
| | 15 | Nishijima Dike | 4.1 | 58.5 | 20.0 | 0.7 | 40.4 | 28.9 | 69.3 | 10.7 | 0.3 |
| | 16 | Upper Niteko Dam | 3.8 | 44.0 | 15.0 | 0.7 | 37.4 | 17.8 | 55.2 | 11.0 | 0.4 |
| | 17 | Middle Niteko Dam | 3.2 | 42.0 | 15.0 | 0.7 | 32.0 | 17.3 | 49.3 | 16.0 | 0.4 |
| | 20 | Idenoshiri Dam | 2.7 | 65.0 | 30.0 | 0.7 | 26.5 | 40.6 | 67.1 | 15.1 | 0.4 |
| | 21 | Jamuna Bridge | 3.0 | 59.0 | 17.0 | 0.7 | 29.5 | 21.5 | 51.1 | 8.4 | |
| | 28 | Tapar Dam | 5.1 | 67.0 | 19.0 | 0.6 | 50.2 | 28.2 | 78.4 | 16.5 | 0.4 |
| | 29 | Fategadh Dam | 5.8 | 102.3 | 19.0 | 0.6 | 57.0 | 29.1 | 86.1 | 17.3 | 0.1 |
| | 30 | Kaswati Dam | 5.9 | 83.0 | 19.0 | 0.6 | 57.9 | 29.2 | 87.1 | 17.5 | 0.4 |
| Current study | | cadia tailings dam | 0.8 | 166.0 | 60.0 | 0.9 | 7.9 | 50.4 | 58.3 | 13.3 | |
| | | Feijiao dam | 1.4 | 174.8 | 55.0 | 0.8 | 13.9 | 51.3 | 65.1 | 14.0 | |
| | | Fundao-Plateau | 10.0 | 139.0 | 12.0 | 0.5 | 99.0 | 13.6 | 112.6 | | 0.1 |
| | | Fundao_slope | 7.5 | 92.4 | 12.0 | 0.6 | 74.3 | 12.3 | 86.6 | 2.8 | 0.1 |
| | | Fundao_Toe | 2.5 | 70.0 | 12.0 | 0.8 | 24.8 | 9.9 | 34.6 | 2.1 | 0.1 |
| | | Palu city | 3.0 | 28.8 | 15.0 | 0.7 | 29.7 | 17.1 | 46.8 | 1.2 | 0.2 |

| | | | | | | | | | | |
|---|---|---|---|---|---|---|---|---|---|---|
| | Las Palas tailings dam | 1.8 | 196.5 | 10.0 | 0.8 | 17.3 | 0.1 | 17.4 | 9.8 | 0.5 |
| | Yamanaka | 4.2 | 76.8 | 28.0 | 0.7 | 41.6 | 41.4 | 83.0 | 7.7 | 0.3 |
| | Kayakari dam | 6.0 | 74.0 | 30.0 | 0.6 | 59.4 | 47.3 | 106.7 | 11.8 | 0.4 |

**Table 7. Results of liquefaction triggering analysis and applicable shear strength ratio for each segment for USFD.**

| Analysis Parameter | **Segment 1 – Upstream Hydraulic Fill** | **Segment 2 – Upstream Hydraulic Fill** | **Segment 3 – Clay Core** | **Segment 4 – Downstream Hydraulic Fill** | **Segment 5 – Downstream Hydraulic Fill** |
|---|---|---|---|---|---|
| Boring | SPT B-1 | SPT B-2 | SPT B-3 | SPT B-4 | SPT B-5 |
| $N_{1,60,cs}$ | 15.1 | 16.8 | - | 15.0 | 15.8 |
| $q_{c1N\text{-}cs}$ | 61.3 | 68.2 | - | 60.9 | 64.1 |
| $FoS_{Liquefaction}$ | 0.4 | 0.6 | - | 0.7 | 1.3 |
| $r_{u,\ seismic}$ (Marcuson et al., 1990) | 0.75 - 1.0 | 0.75 - 1.0 | - | 0.75 - 1.0 | 0.04 - 0.35 |
| $r_{u,\ seismic}$ (Piezometric data) | N/A | Overflowed (P1) | Overflowed (P2) | N/A | 0.12 (P3) |
| Applicable strength ratio | Liquefied strength ratio | Liquefied strength ratio | Yield strength ratio | Liquefied strength ratio | Yield strength ratio |

**Table 8. Pore pressure generation for Fundão tailings dam.**

| Local Time | Magnitude (Mw) | Pga (g) | $Sand_{slope}$ ($FoS_{liquefaction}/r_{ustatic}$) | $Sand_{plateau}$ ($FoS_{liquefaction}/r_{ustatic}$) | $Sand_{Toe}$ ($FoS_{liquefaction}/r_{ustatic}$) |
|---|---|---|---|---|---|
| 14:12 | 2.2 | 0.06 | 2.1/0.14 | 2.9/0.07 | 1.8/0.15 |
| 14:13 | 2.6 | 0.08 | 1.6/0.26 | 2.2/0.11 | 1.5/0.28 |
| 14:16 | 1.8 | 0.06 | 2.1/0.14 | 2.9/0.07 | 1.8/0.15 |
| Total $R_{u,seismic}$ | | | NA/0.54 | NA/0.25 | NA/0.58 |

## FIGURE CAPTIONS

**Fig. 1. Schematic undrained response of saturated sandy soil subjected to static and dynamic loads.**

**Fig. 2. Empirical correlation between effective normal stress and normalized CPT tip resistance for static flow failure case histories shown in Table 1.**

**Fig. 3. Empirical correlation between effective normal stress and normalized clean sand CPT tip resistance for static flow failure case histories shown in Table 2.**

**Fig. 4. Empirical correlation between $q_{c1}$ (bars indicate range of penetration test values) and pre-failure effective vertical stresses for static and seismic case histories.**

**Fig. 5. Empirical correlation between $q_{c1N\text{-}cs}$ and pre-failure effective vertical stresses for static and seismic case histories.**

**Fig. 6. Relationship between factor of safety against liquefaction and seismic residual excess pore-water pressure ratio. Red data point shows the $FoS_{Liquefaction}$ and corresponding $r_{u,seismic}$ for USFD example.**

**Fig. 7. Empirical correlation between $S_u(_{Liquefaction})/\ \sigma'_{vo}$ and corrected cone penetration tip resistance from flow failures.**

**Fig. 8. Empirical correlation between $S_u(_{Liquefaction})/\ \sigma'_{vo}$ and corrected clean sand cone penetration tip resistance from flow failures.**

**Fig. 9. Empirical correlation between $S_u(_{yield})/\ \sigma'_{vo}$ and corrected cone penetration tip resistance from static flow failures.**

**Fig. 10. Change in piezometric levels during and after the 1971 San Fernando earthquake (data from Serff et al., 1976).**

**Fig. 11. Cross-section showing location of relevant soil borings, zones of hydraulic sand fills, piezometers just before deformations, and five segments along estimated failure surface.**

**Fig. 12. Summary of available pre-earthquake SPT data showing corrected $N_{1,60,cs}$ values: (a) segments 1 and 2 (b) segments 4 and 5 (data from Serff et al., 1976).**

**Fig. 13. Comparison of instability line, critical state locus, and reduction in effective stress of segment 5 due to seismically induced pore-water using the piezometric data in P3.**

**Fig. 14. Available CPT data showing corrected $q_{c1N\text{-}cs}$ values: (a) CPT 5 (b) CPT 6 (modified from Bardet and Davis, 1996)**

**Fig. 15. Cross-Section 02 showing location of relevant cone penetration tests, soil borings, zones of loose sand tailings, and field observations of scarp formation and toe cracking and seepage at failure (after Stark et al. (2023)).**

**Fig. 16. Comparison of CSRL, IL, and reduction in effective stress due maximum seismically induced pore-water pressures from Marcuson et al. (1990) for the left abutment: (a) downstream slope, $Sand_{Slope}$, (b) plateau area, $Sand_{Plateau}$, and (c) downstream, $Sand_{Toe}$.**

## FIGURES

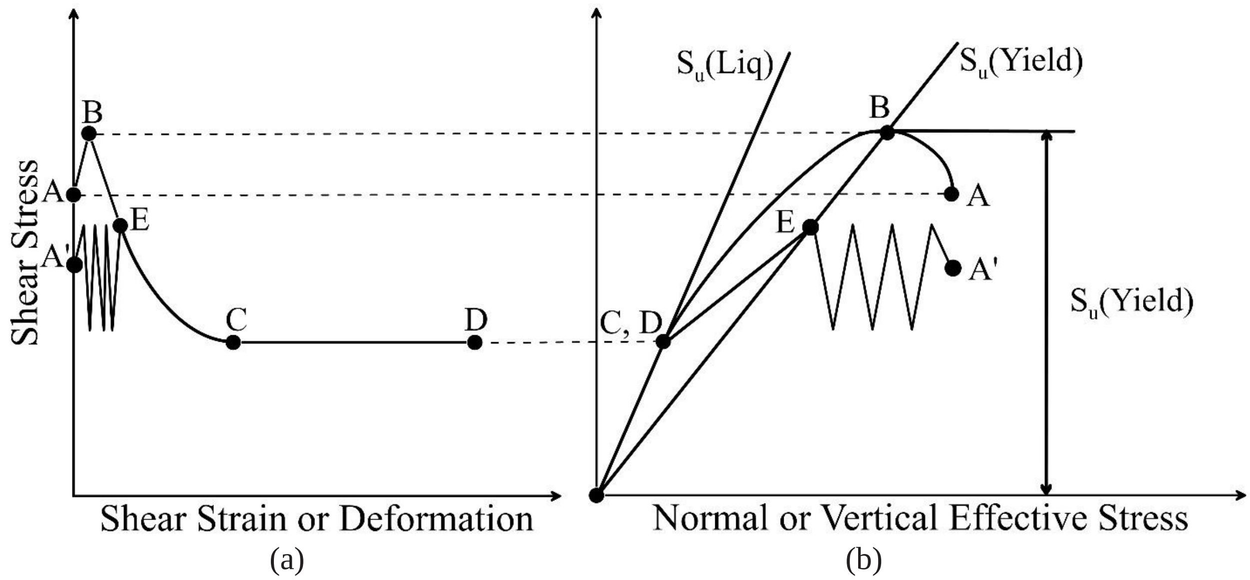


**Fig. 1. Schematic undrained response of saturated sandy soil subjected to static and dynamic loads.**

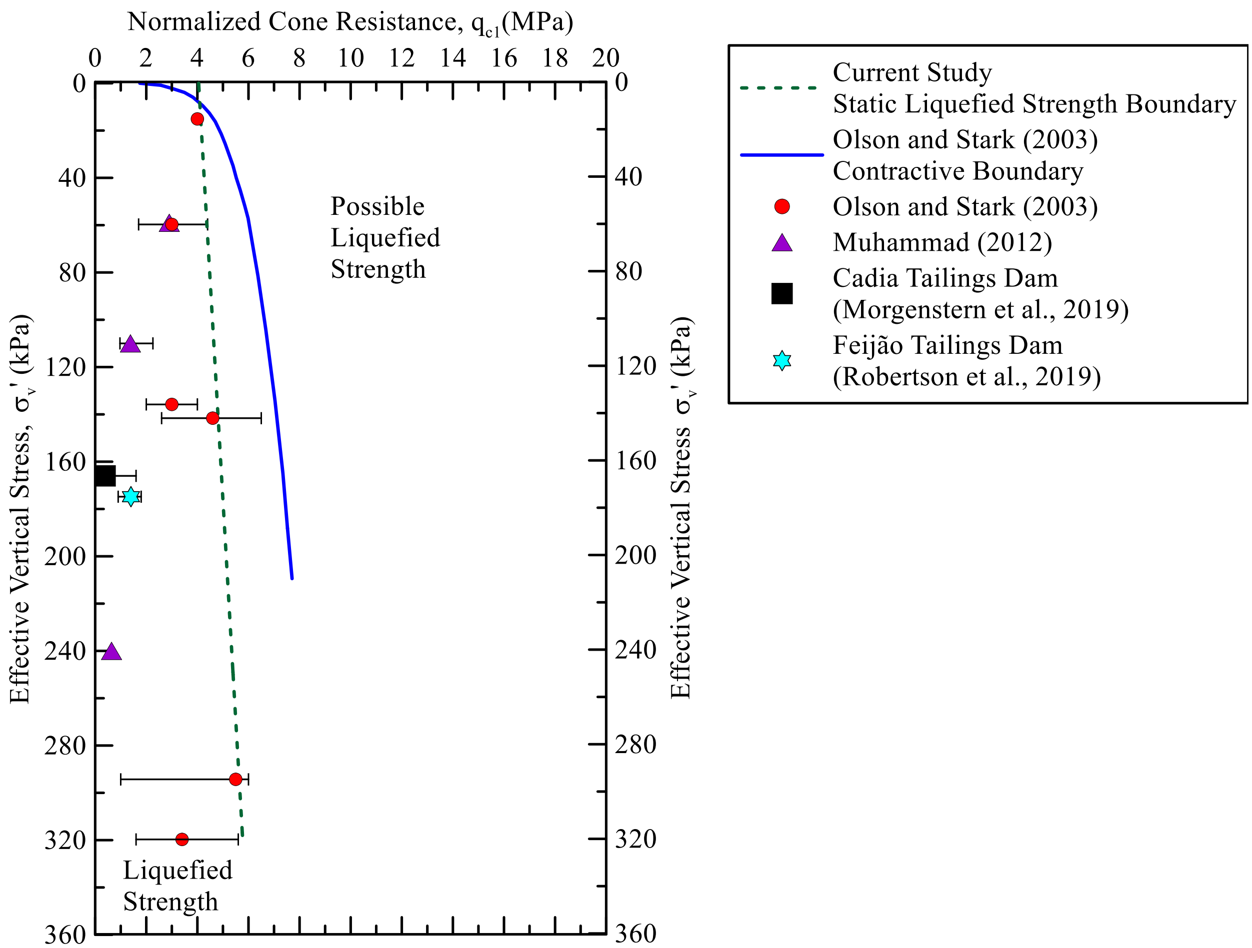


**Fig. 2.** **Empirical correlation between effective normal stress and normalized CPT tip resistance without fines content correction for static flow failure case histories shown in Table 1.**

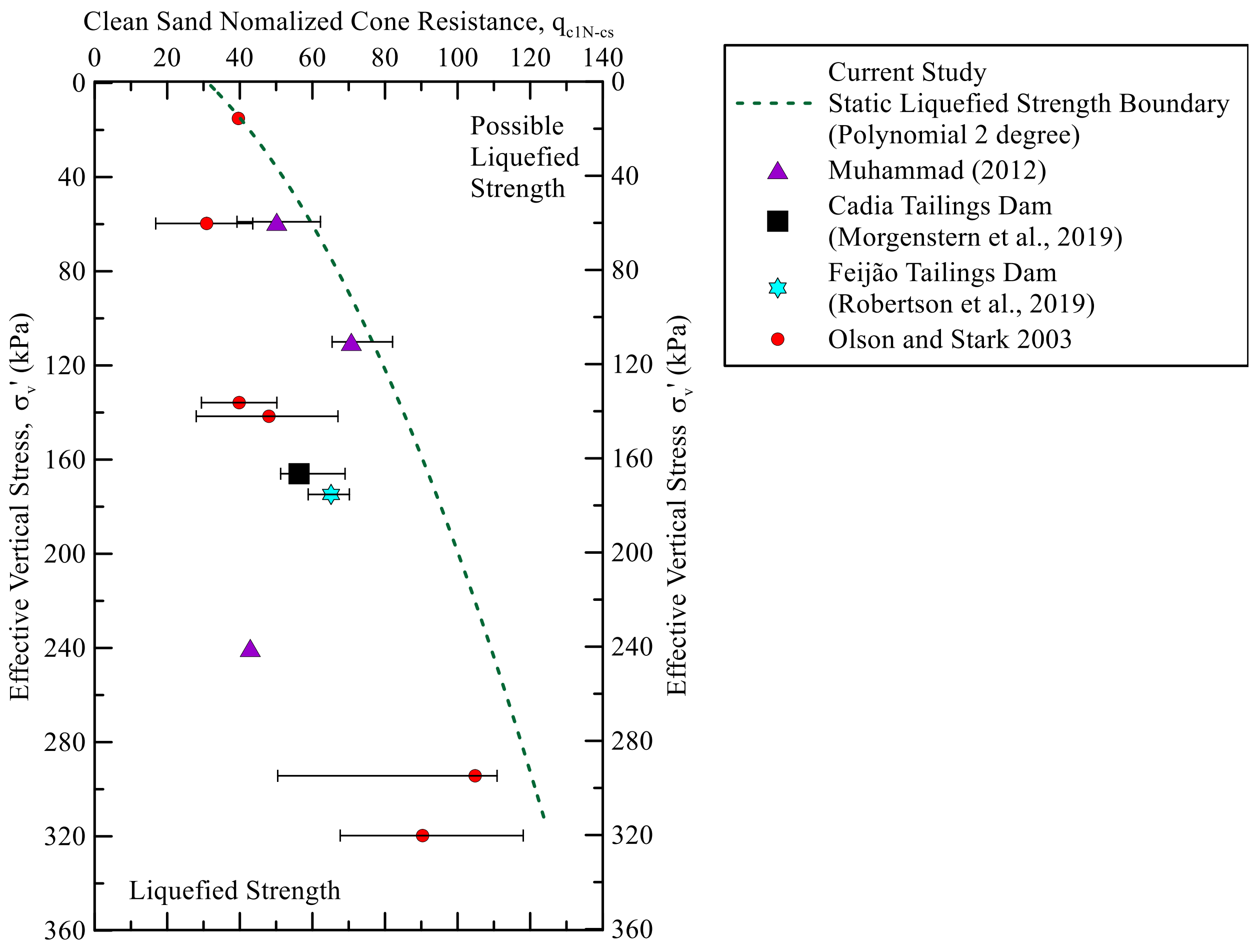


**Fig. 3.** **Empirical correlation between effective normal stress and normalized clean sand CPT tip resistance for static flow failure case histories shown in Table 2.**

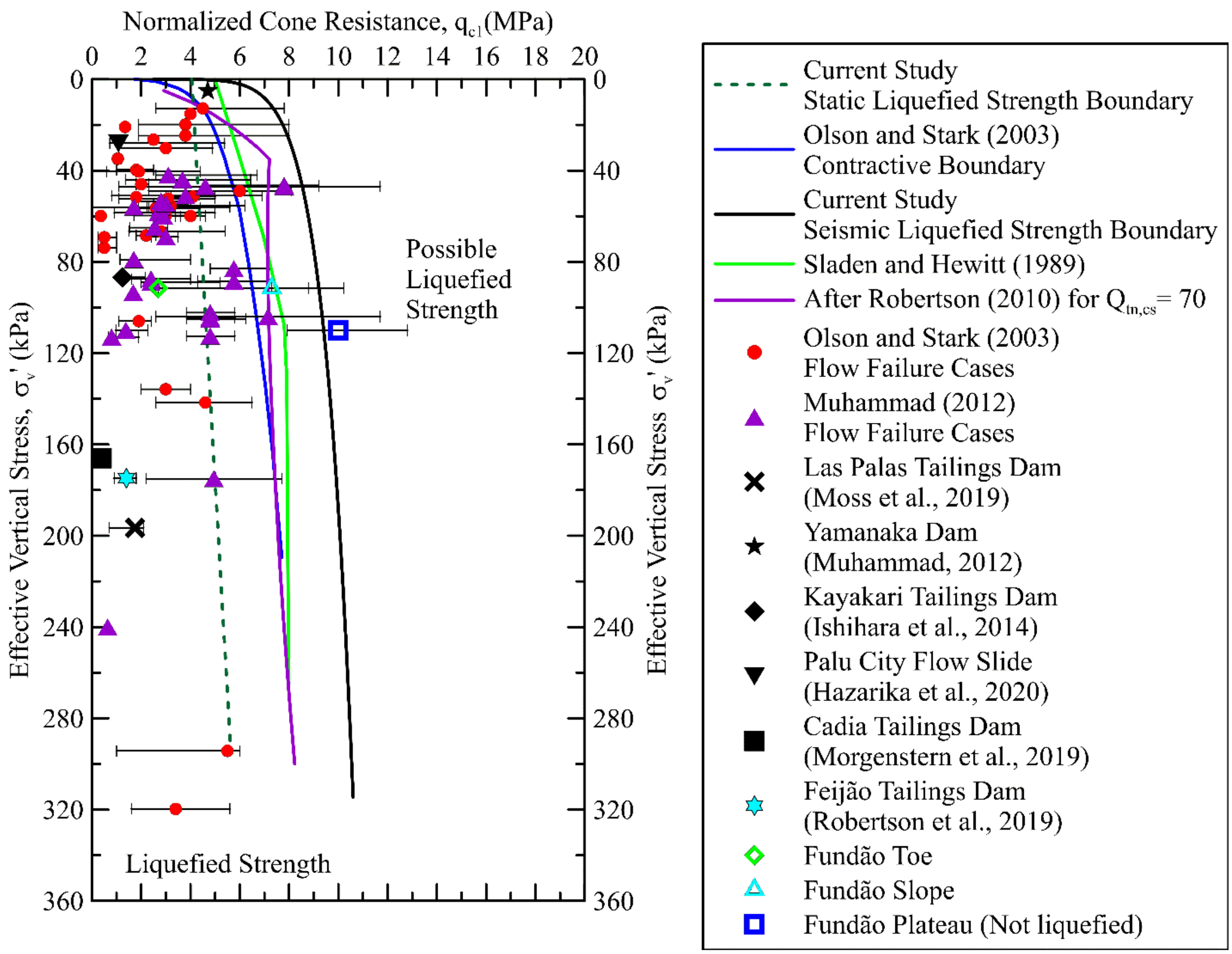


**Fig. 4.** **Empirical correlation between $q_{c1}$ (bars indicate range of penetration test values) and pre-failure effective vertical stresses without fines content correction for static and seismic flow slide case histories.**

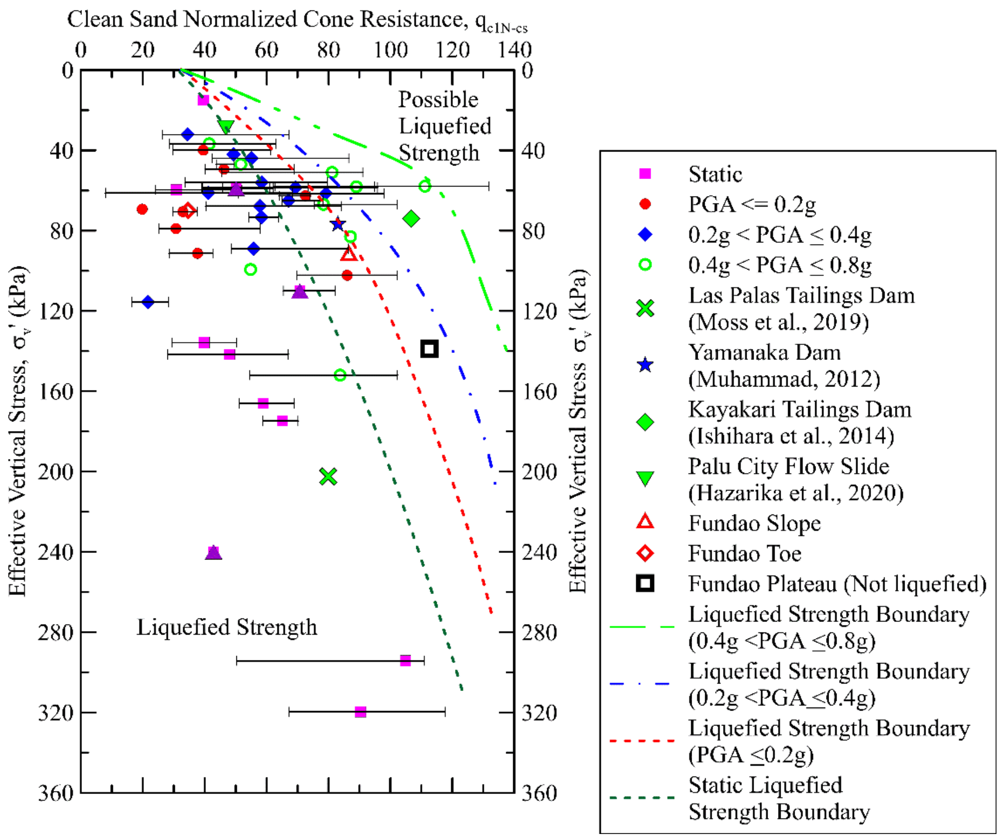


**Fig. 5.** **Empirical correlation between $q_{c1N\text{-}cs}$ and pre-failure effective vertical stresses for static and seismic flow slide case histories.**

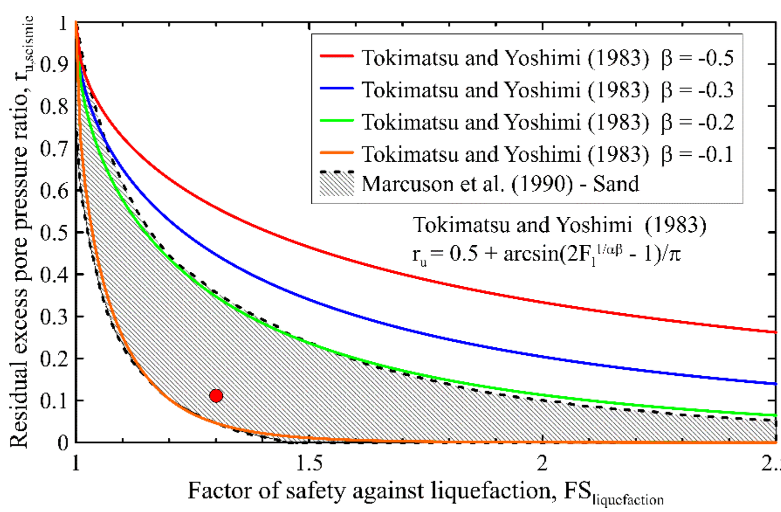


**Fig. 6.** **Relationship between factor of safety against liquefaction and seismic residual excess pore-water pressure ratio and red data point shows the $FoS_{Liquefaction}$ and red dot corresponding $r_{u,seismic}$ for USFD example.**

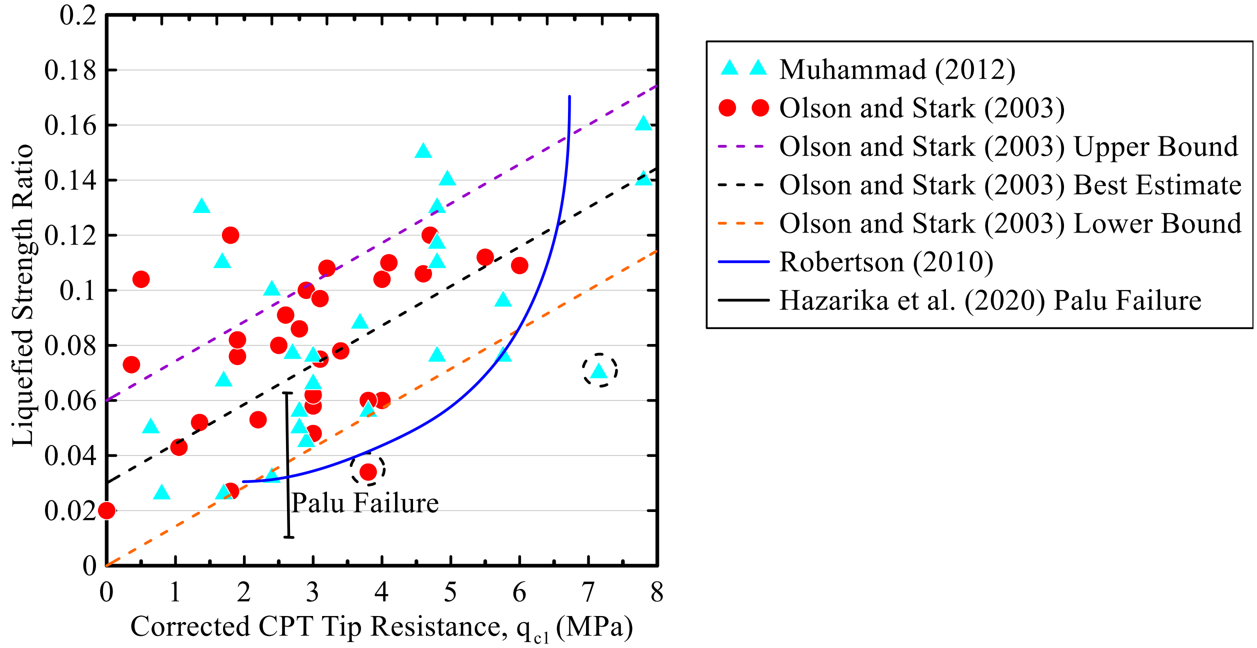


**Fig. 7.** **Empirical correlation between $S_u$(Liquefaction)/ $\sigma'_{vo}$ and corrected cone penetration tip resistance from flow failures.**

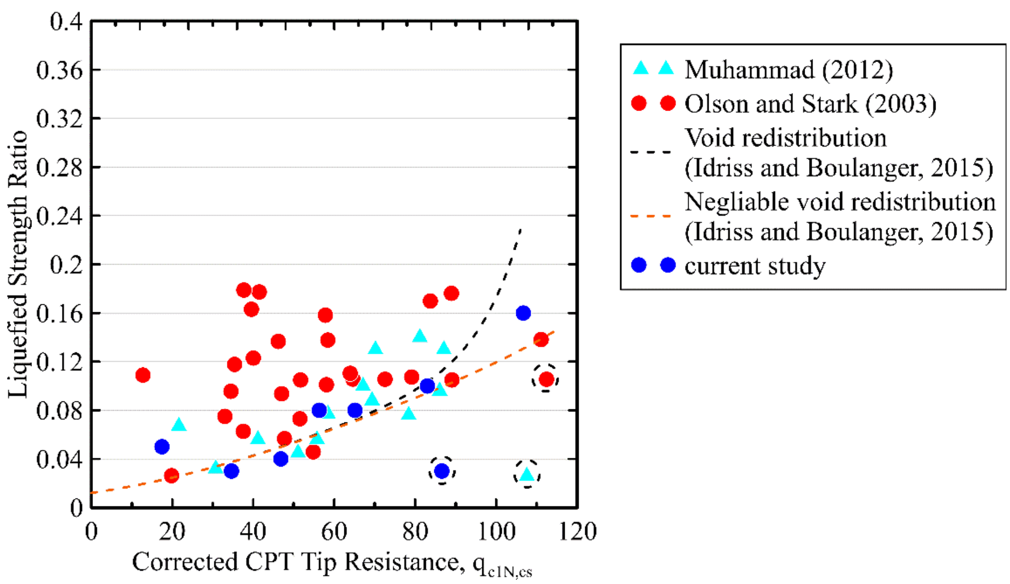


**Fig. 8.** **Empirical correlation between $S_u$(Liquefaction)/ $\sigma'_{vo}$ and corrected clean sand cone penetration tip resistance from flow failures.**

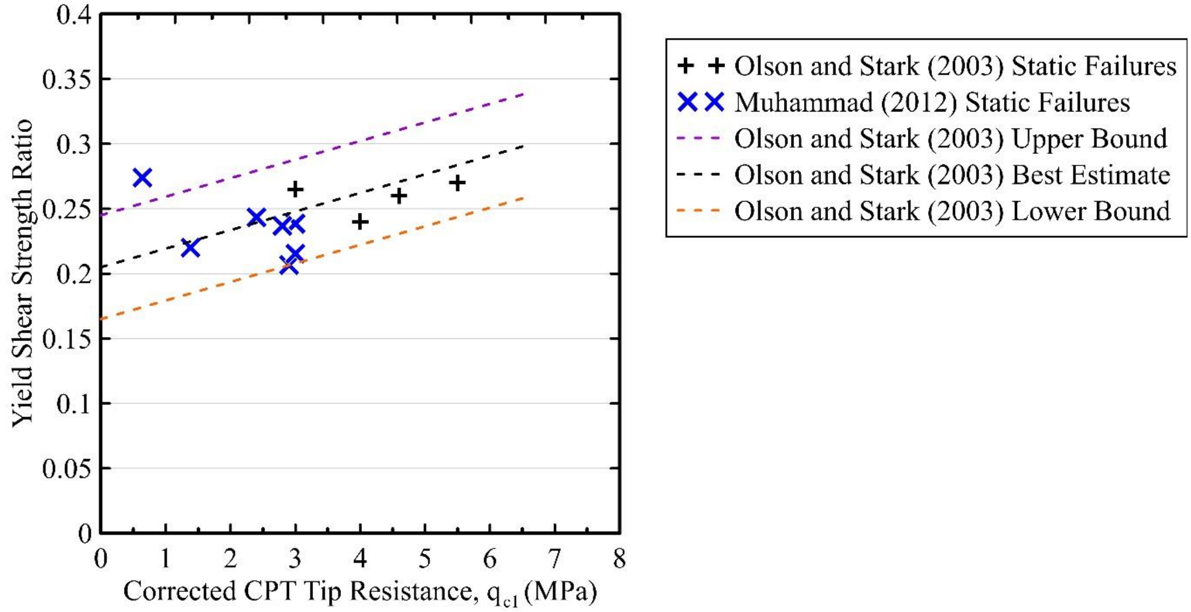


**Fig. 9.** **Empirical correlation between $S_{u(yield)}/\sigma'_{vo}$ and corrected cone penetration tip resistance from static flow failures.**

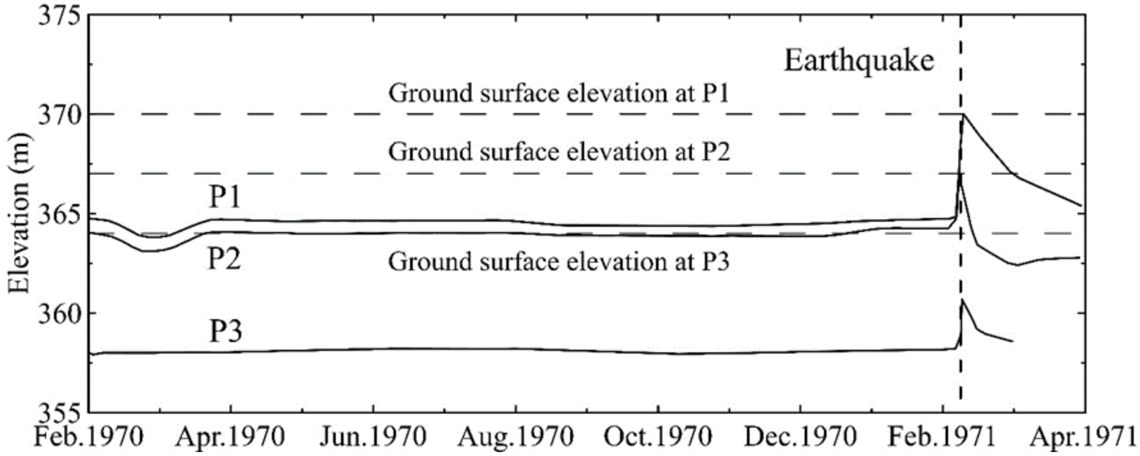


**Fig. 10.** **Change in piezometric levels during and after the 1971 San Fernando earthquake (data from Serff et al., 1976).**

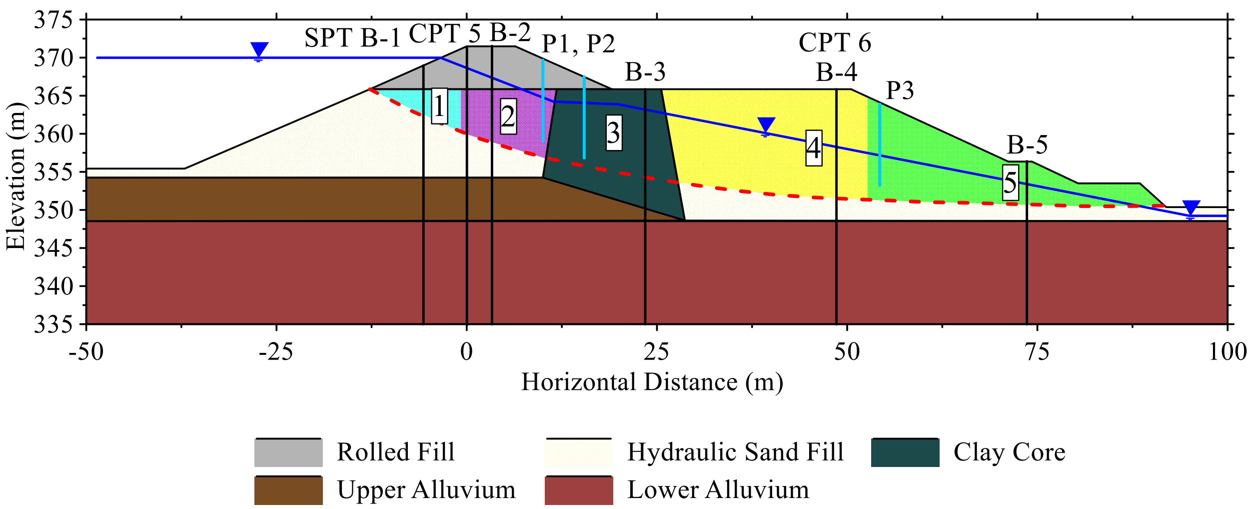


**Fig. 11.** **Cross-section showing location of relevant soil borings, zones of hydraulic sand fills, piezometers just before deformations, and five segments along estimated failure surface.**

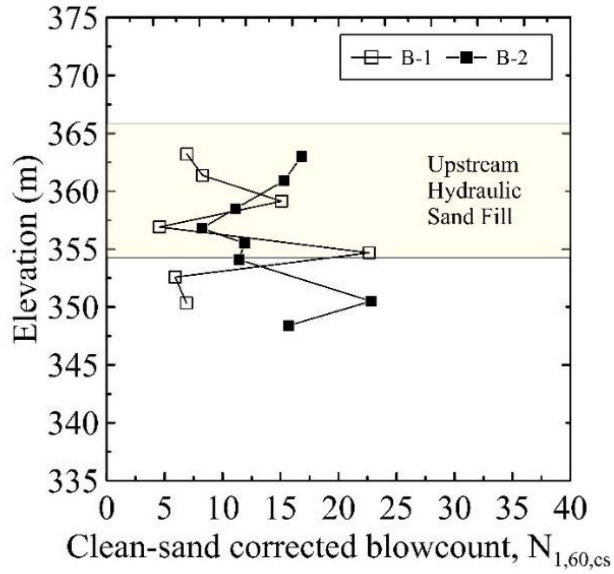


(a)

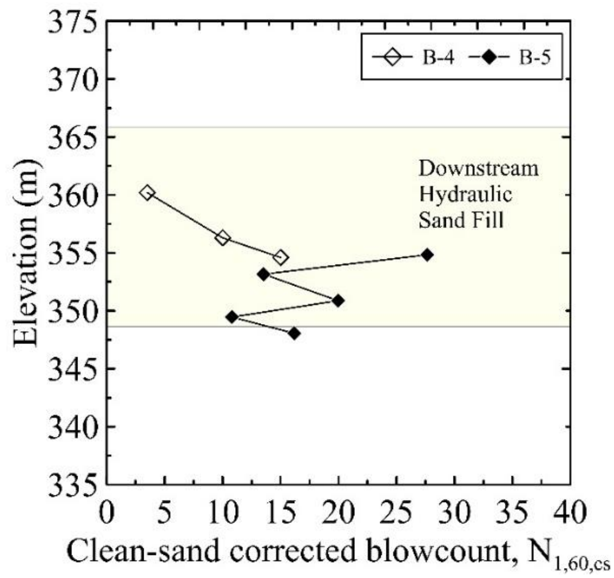


(b)

**Fig. 12.** **Summary of available pre-earthquake SPT data showing corrected $N_{1,60,cs}$ values: (a) segments 1 and 2 (b) segments 4 and 5 (data from Serff et al., 1976).**

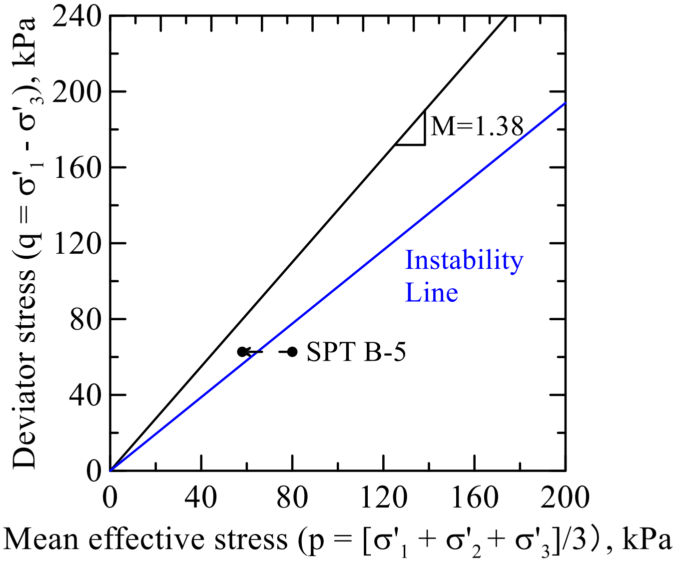


**Fig. 13.** **Comparison of instability line, critical state locus, and reduction in effective stress of segment 5 due to seismically induced pore-water using the piezometric data in P3.**

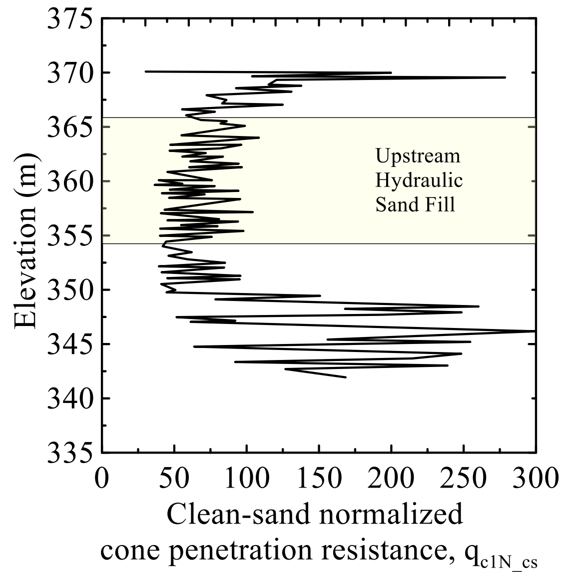


(a)

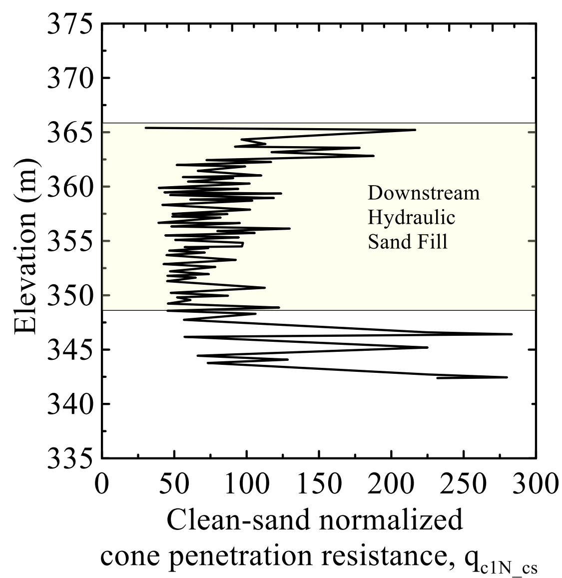


(b)

**Fig. 14.** **Available CPT data showing corrected $q_{c1N-cs}$ values: (a) CPT 5 (b) CPT 6 (modified from Bardet and Davis, 1996)**

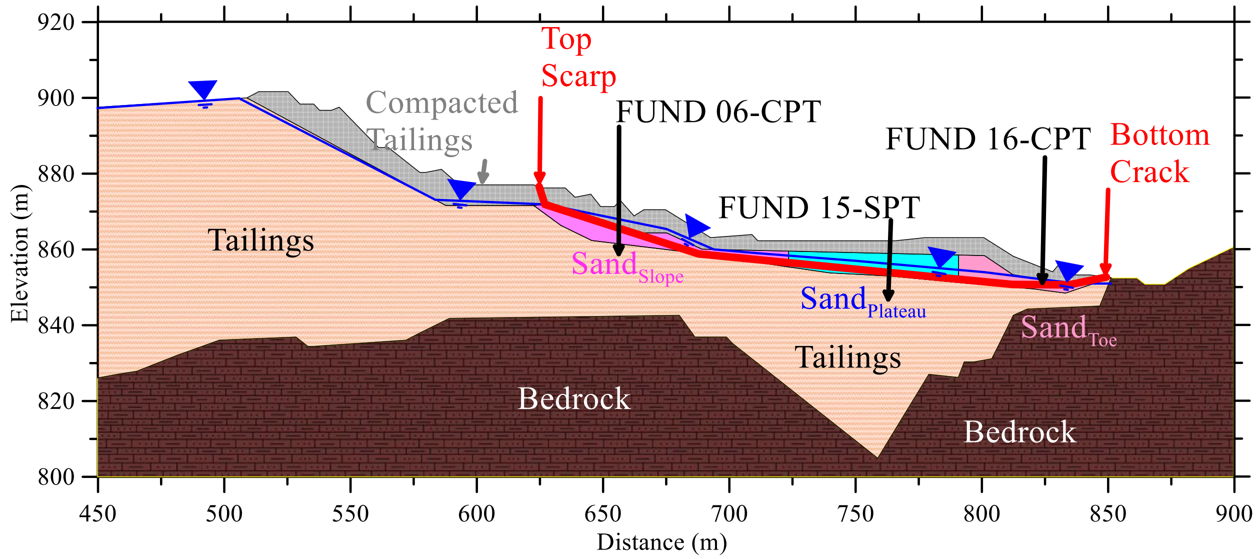


**Fig. 15.** **Cross-Section 02 showing location of relevant cone penetration tests, soil borings, zones of loose sand tailings, and field observations of scarp formation and toe cracking and seepage at failure (after Stark et al. (2023)).**

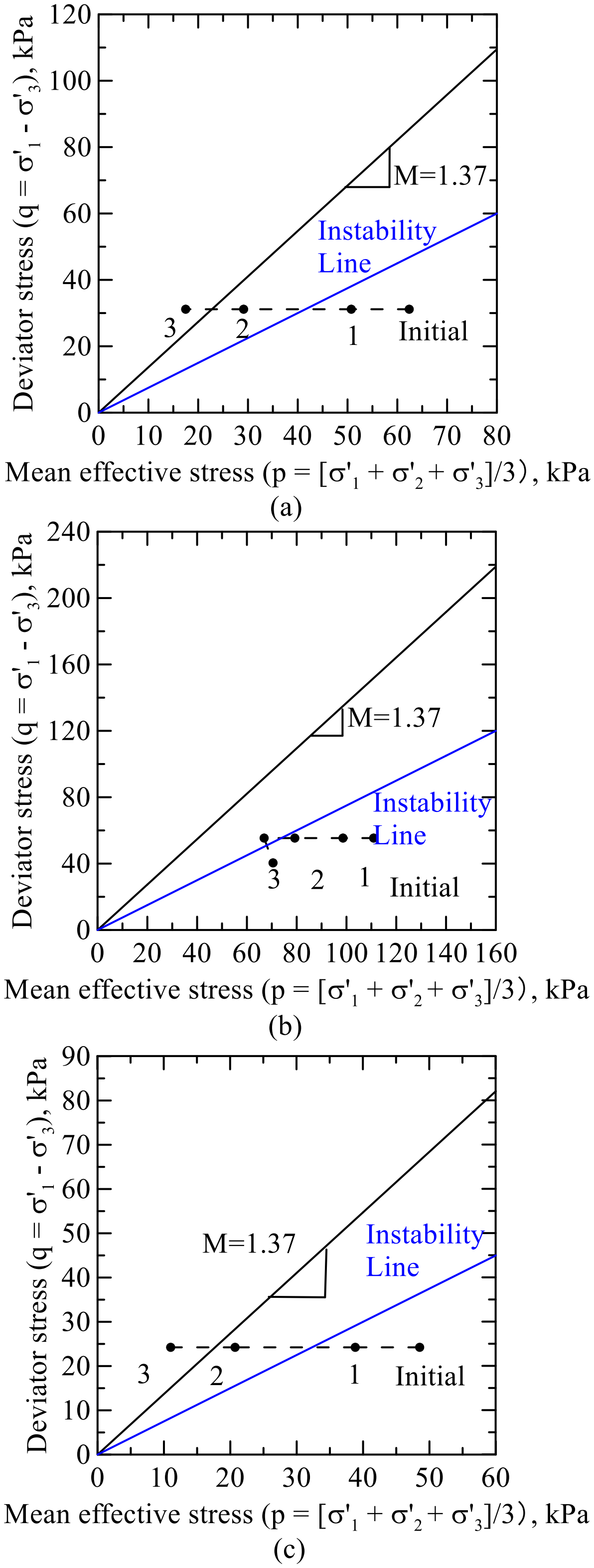


**Fig. 16. Comparison of CSRL, IL, and reduction in effective stress due maximum seismically induced pore-water pressures from Marcuson et al. (1990) for the left abutment: (a) downstream slope, $Sand_{Slope}$, (b) plateau area, $Sand_{Plateau}$, and (c) downstream, $Sand_{Toe}$.**